nature communications

Article

https://doi.org/10.1038/s41467-024-44739-9

# Localisation-to-delocalisation transition of moiré excitons in $WSe_2/MoSe_2$ heterostructures

Received: 24 April 2023

Accepted: 2 January 2024

Published online: 05 February 2024

Check for updates

Elena Blundo[1] ✉, Federico Tuzi[1], Salvatore Cianci[1], Marzia Cuccu[1], Katarzyna Olkowska-Pucko[2], Łucja Kipczak[2], Giorgio Contestabile[1], Antonio Miriametro[1], Marco Felici[1], Giorgio Pettinari[3], Takashi Taniguchi[4], Kenji Watanabe[5], Adam Babiński[2], Maciej R. Molas[2] & Antonio Polimeni[1] ✉

Moiré excitons (MXs) are electron-hole pairs localised by the periodic (moiré) potential forming in two-dimensional heterostructures (HSs). MXs can be exploited, e.g., for creating nanoscale-ordered quantum emitters and achieving or probing strongly correlated electronic phases at relatively high temperatures. Here, we studied the exciton properties of $WSe_2/MoSe_2$ HSs from $T = 6$ K to room temperature using time-resolved and continuous-wave microphotoluminescence also under a magnetic field. The exciton dynamics and emission lineshape evolution with temperature show clear signatures that MXs de-trap from the moiré potential and turn into free interlayer excitons (IXs) for temperatures above 100 K. The MX-to-IX transition is also apparent from the exciton magnetic moment reversing its sign when the moiré potential is not capable of localising excitons at elevated temperatures. Concomitantly, the exciton formation and decay times reduce drastically. Thus, our findings establish the conditions for a truly confined nature of the exciton states in a moiré superlattice with increasing temperature and photo-generated carrier density.

Two-dimensional (2D) heterostructures (HSs) can be formed by stacking two (or more) monolayers (MLs) of different van der Waals crystals. 2D HSs offer a countless number of combinations thanks to the nearly arbitrary choice of the chemical composition of the individual constituents and the control of their relative angular alignment given by the twist angle $\theta$[1]. Inherent to the stacking process is the formation of a moiré superlattice that superimposes on the topographic and electronic structure of the single MLs. This phenomenon has been particularly investigated in HSs made of transition metal dichalcogenide (TMD) semiconductors, which feature a sizeable band gap[2–8]. The moiré potential can be as deep as 100 meV[3,4,7] and can localise both intralayer excitons (Xs) residing in the MLs of the HS[9] and interlayer excitons (IXs)[3–6] and trions[10], in which different charge carriers reside in the different layers of the HS. Moiré-confined IXs (hereafter, moiré excitons, MXs) are especially interesting as they can be exploited as nanoscale-ordered arrays of quantum emitters[3,11]. Furthermore, their space-indirect character endows IXs, and specifically MXs, with long lifetimes[4,5] that, in conjunction with the depth of the moiré potential, make them suitable for the observation of high-temperature (>100 K) Bose-Einstein condensates, as shown in a $WSe_2/MoSe_2$ HS[12]. The topology of the moiré potential also induces strongly correlated electron and exciton states[13,14] that led to the observation of an exciton insulator surviving up to 90 K in a $WS_2$/bilayer-$WSe_2$ HS[15]. In addition, the MXs themselves were employed as a probe of the

[1]Physics Department, Sapienza University of Rome, Piazzale Aldo Moro 5, 00185 Rome, Italy. [2]Institute of Experimental Physics, Faculty of Physics, University of Warsaw, Pasteura 5, 02-093 Warsaw, Poland. [3]Institute for Photonics and Nanotechnologies, National Research Council, 00133 Rome, Italy. [4]International Center for Materials Nanoarchitectonics, National Institute for Materials Science, 1-1 Namiki, Tsukuba 305-0044, Japan. [5]Research Center for Functional Materials, National Institute for Materials Science, 1-1 Namiki, Tsukuba 305-0044, Japan. ✉e-mail: elena.blundo@uniroma1.it; antonio.polimeni@uniroma1.it

existence of Mott insulators and Wigner crystals in $WSe_2/WS_2$ HSs at relatively large temperatures[16,17].

For boson condensates and highly correlated charge systems, as well as quantum photonics applications, the thermal stability of the moiré-induced confinement of the excitons plays a crucial role and a fundamental question arises: Up to what extent can MXs be regarded as truly moiré-confined?

In this work, we addressed this important aspect by investigating the effects of the lattice temperature and of the photo-generated exciton density on the localisation of MXs, as resulting from their: (i) luminescence intensity and lineshape, (ii) temporal dynamics, (iii) magnetic moments. Specifically, we studied the emission properties of two exemplary $WSe_2/MoSe_2$ HSs by continuous-wave (cw) micro-photoluminescence ($\mu$-PL) measurements, also under magnetic field, and by time-resolved (tr) $\mu$-PL. Low-temperature ($T = 6$ K) tr-$\mu$-PL shows that the MX signal is characterised by different spectral components, with formation and recombination dynamics indicative of the presence of a multi-level electronic potential[4,6,18,19], as well as of MXs localised at minima with different atomic registry as apparent from their gyromagnetic factor[20]. The temperature evolution of the HS emission properties presents clear signatures of IX de-trapping from the moiré potential at $T$s above 100 K and the ensuing spectral predominance of free IXs at higher temperatures. Concomitantly, Zeeman-splitting measurements reveal an unexpected sign reversal of the exciton magnetic moment taking place with the temperature-induced MX transition to a free IX regime. This transition is paralleled by a strong reduction of both the emission rise and decay times, which mirrors the faster formation and recombination dynamics, respectively, of the free IXs.

## Results

### Moiré exciton dynamics at low temperature

The two investigated $WSe_2/MoSe_2$ HSs were fabricated by depositing the first ML on the substrate (directly on a $SiO_2$/Si substrate in one HS, and on a h-BN flake deposited on a $SiO_2$/Si substrate in the other HS) and by then depositing the second ML on top. The HSs were then capped with a thin h-BN layer; see Methods for other details. A comparison of the PL properties before and after the h-BN capping (see Supplementary Note 1) did not show sizeable variations of the HS optical properties. Both HSs are characterised by a rather homogeneous PL signal, both in terms of lineshape and intensity, see Supplementary Note 1. The twist angle between the $MoSe_2$ and $WSe_2$ MLs was estimated to be $\theta = 0.46^\circ$ in the first HS (hereafter HS1) and $0.74^\circ$ in the second (hereafter HS2), as detailed next. Such angles are close to $0^\circ$ and correspond to the configuration referred to as R-type (while HSs with $\theta$ close to $60^\circ$ are named H-type). We will discuss mainly the results obtained on HS1 with $\theta = 0.46^\circ$ and refer to HS2 ($\theta = 0.74^\circ$) as a comparative case. Figure 1a shows an optical microscope image of HS1 along with its sketch. Cw and tr-$\mu$-PL measurements were carried out at variable laser excitation power $P_{exc}$ and temperature using a confocal microscope setup. For $\mu$-PL excitation ($\mu$-PLE) measurements, we employed the same setup using a wavelength-tunable laser as excitation source. Magneto-$\mu$-PL measurements were performed at variable temperature in a superconducting magnet up to 16 T, with the field perpendicular to the HS plane. Further details are reported in the Methods section.

Figure 1 b shows the $T = 6$ K $\mu$-PL spectrum (wine line) of HS1. Two bands are observed. The one peaked at 1.6 eV, labelled X, is due to a group of localised (intralayer) exciton states originating from the $MoSe_2$ ML with a small contribution from similar transitions in the $WSe_2$ ML on the higher energy side of the band. The band centred at ≈ 1.36 eV, labelled MX, is due to MX recombination (with the electron and hole being confined in the $MoSe_2$ and $WSe_2$ layer, respectively), as also reported in other works[4,6,7,13]. The blue line in Fig. 1b is the $\mu$-PLE spectrum obtained by monitoring the MX signal while scanning the excitation laser wavelength. The MX signal shows a resonant contribution from the $MoSe_2$ and $WSe_2$ ML exciton states of the HS, thus confirming the interlayer nature of the MX band. We point out that, at variance with ref. 21, no MX-related absorption feature is instead observed in the $\mu$-PLE data due to the much smaller oscillator strength of the MX absorption. Figure 1c displays the MX spectrum recorded at $T = 6$ K with $P_{exc} = 5$ nW (corresponding to 0.64 W/cm$^2$). The spectrum can be deconvolved into several Gaussian components. The latter are equally spaced by (12.8 ± 1.3) meV, reflecting the quantised states of the moiré potential[4,6,18,19]. The Gaussian lineshape maps onto the ensemble of MXs confined in randomly distributed moiré minima, due to the inevitable imperfections present in the HS plane. The very narrow lines superimposed on the multi-Gaussian lineshape of the MX band likely correspond to single MXs confined in just one moiré minimum[7,22]. The centroid energy of the MX band (1.357 eV) indicates that the investigated HS is R-type ($\theta \approx 0^\circ$)[4–6,13,23] with $R_h^X$ local atomic registry[3,7]. In fact, for H-type HSs ($\theta \approx 60^\circ$) the MX

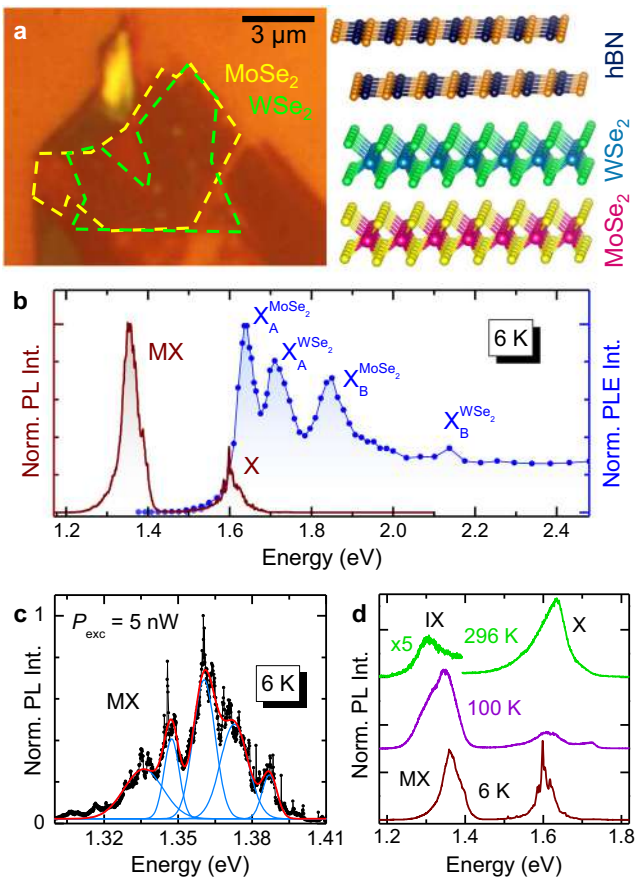


**Fig. 1 | Optical properties of the $WSe_2/MoSe_2$ R-type HS1. a** Optical micro-graph (left) and sketch (right) of HS1. **b** Low-$T$ $\mu$-PL and $\mu$-PLE spectra of the HS, left and right axis, respectively. In the $\mu$-PL spectrum ($P_{exc} = 2$ $\mu$W), X indicates the intralayer exciton recombination from localised states of the $MoSe_2$ and $WSe_2$ monolayers (lower- and higher-energy side, respectively). MX is the moiré exciton band. In the $\mu$-PLE spectrum, four exciton resonances are observed. These resonances can be attributed to the A and B excitons (where the hole sits in the upper, A, and lower, B, spin-split valence band maximum at K, and the electron sits in the spin-split conduction band minimum at K with same spin) of the $MoSe_2$ and $WSe_2$ layers. **c** $\mu$-PL spectrum of the MX band acquired with very low laser power excitation (5 nW). The spectrum can be reproduced by five Gaussian functions (azure: single components; red line: total fit) that are spaced by (12.8 ± 1.3) meV. The very narrow lines that make up the broader Gaussian peaks correspond to single MXs recombining in moiré minima. **d** $\mu$-PL spectra recorded at different temperatures (and $P_{exc} = 20$ $\mu$W). The moiré/interlayer (MX/IX) exciton band is visible up to room temperature. X indicates the exciton band related to the single layer $MoSe_2$ and $WSe_2$ constituents of the HS.

https://doi.org/10.1038/s41467-024-44739-9

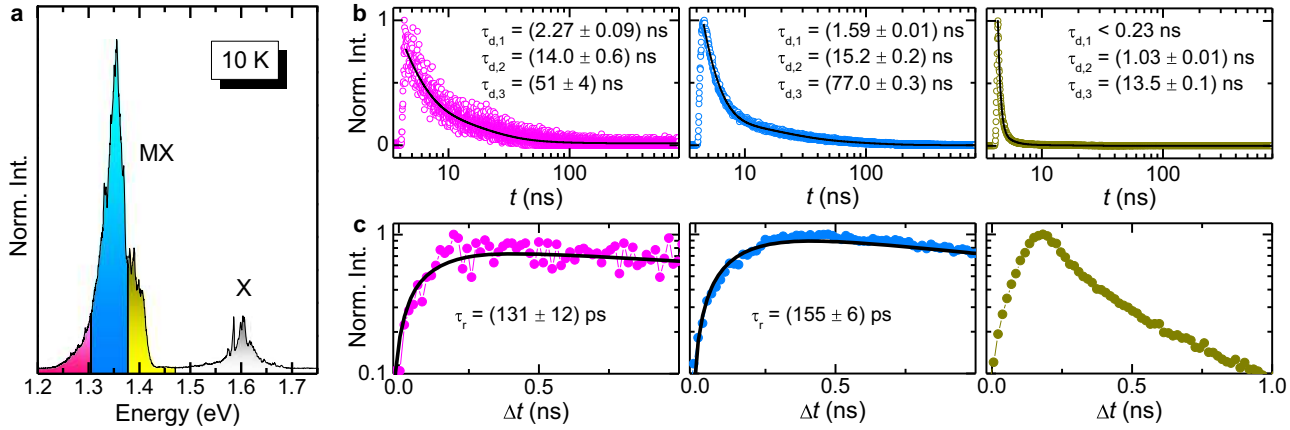


**Fig. 2 | Decay and rise of the moiré exciton band. a** $T = 10$ K and $P_{exc} = 1$ μW μ-PL spectrum of HS1. MX indicates the moiré-trapped interlayer exciton, and X indicates the intralayer exciton recombination. Three different spectral regions are highlighted on the MX band. On each of these regions, the μ-PL time evolution was recorded. **b** Time-evolution of the μ-PL signal recorded in the Δt = 0-800 ns interval from the laser pulse on the three spectral regions highlighted in panel **a** (note also the colour code). The decay time $\tau_{d,n}$ values obtained by fitting the data via Eq. (1) (see solid lines) are displayed. **c** The same as **b** for Δt = 0–1.0 ns. The rise time $\tau_r$ values displayed in the panels are those used to reproduce the data with Eq. (2) (see solid lines). The data in the right-most panel could not be fitted reliably.

recombination is centred at a higher energy −by about 40 meV[3,5,7,10,11,22,24–31]— due to the shallower moiré potential for H-type HSs with respect to R-type HSs[7], see also Supplementary Note 1. From the spacing between the MX states, as detailed in Supplementary Note 2, we estimate a moiré superlattice period $a_m$ of about 40 nm, which corresponds to $\theta = \left(0.46^{+0.05}_{-0.04}\right)^{\circ}$[10]. Second harmonic generation (SHG) measurements confirm that estimation and provide $\theta = 0.1^{\circ} \pm 1.5^{\circ}$, as reported in Supplementary Note 2. Given the large uncertainty of the SHG data, we will assign to this HS the twist angle $\theta = 0.46^{\circ}$, determined by the energy spacing of the moiré potential resonances. From the HS period, we deduce that about 600 moiré minima are probed within the laser spot (radius equal to ≈ 500 nm). The excellent alignment leads to a sizeable signal of the HS IXs up to room temperature, as shown in Fig. 1d. Note that the recombination from the HS is indicated as MX at $T$ = 6 K and as IX at $T$ = 296 K, qualitatively hinting at a temperature-induced transition in the character of the exciton. We investigated such transition by studying the temporal evolution of the HS exciton signal, its dependence on the number of photo-generated carriers and by determining the exciton gyromagnetic factor at different temperatures and photo-generated carrier densities.

We first describe the tr-μ-PL results at $T = 10$ K, where most of the HS emission is due to the MX recombination in the $R^X_h$ minima of the moiré potential[3,7,32]. Figure 2a shows the μ-PL spectrum of HS1 recorded at a power 200 times larger ($P_{exc}$=1 μW, i.e., 128 W/cm$^2$) than in Fig. 1c. This results in a non negligible contribution from a component centred at about 1.4 eV, which can be assigned (totally or partly) to moiré excitons confined in the $R^h_h$ minima (as confirmed later). Indeed, the energy distance between this contribution and the lowest energy component (1.335 eV) of the HS emission at very low power density (see Fig. 1c) is about 65 meV. This value falls within the range of the band gap energy difference between the $R^X_h$ and $R^h_h$ moiré evaluated in refs. 3 (40 meV) and ref. 4 (70 meV). Three different spectral windows are highlighted in Fig. 2a. For each of them, panel b and panel c display the corresponding μ-PL signal time evolution from the laser pulse up to 800 ns and in the time interval (0-1) ns, respectively (see also Supplementary Note 3, where the same data are compared to the laser pulse setting the resolution limit of our optical system). In the former range, the decay part of the data can be fitted by

$$I_{decay}(t) = \sum_{n=1}^{3} A_{d,n} \cdot \exp\left(-\frac{t - t_0}{\tau_{d,n}}\right), \quad (1)$$

where $t_0$ is a reference time (from which the decay starts), and $\tau_{d,n}$ is the decay time relative to the $n$-th component, whose weight is given by $w_{d,n} = A_{d,n}/(A_{d,1} + A_{d,2} + A_{d,3})$. The fitting curves are superimposed to the data as solid lines in Fig. 2b and the $\tau_{d,n}$ values are displayed in the same figure (the complete set of the fitting parameters, including $w_{d,n}$, can be found in Supplementary Note 3). The presence of different components (1, 2 and 3) indicates that different intermediate and intercommunicating levels are involved in the MX decay, possibly including dark exciton states[6,19]. In any case, $\tau_{d,n}$ gets shorter for the higher energy ranges considered; this is particularly true for the 1.4 eV component, similar to recent results[4,6,13,19]. This finding supports the hypothesis that the structured MX emission corresponds to a ladder of discrete states arising from the moiré potential[4,6,19]. Indeed, higher-energy states may decay faster (due to the tendency of photo-generated carriers to occupy lower-lying states), with the ground state having the longest lifetime of several tens of ns, consistent with the spatially and k-space indirect characteristics of the MX transition. We recall that in TMD MLs the intralayer exciton X is known to have much shorter radiative decay times, on the order of a few ps to a few of tens of ps[33,34], in contrast with MX. A similar behaviour is found in the second $WSe_2/MoSe_2$ HS investigated, or HS2, with energy spacing between the moiré resonances equal to (20.3 ± 3.4) meV and twist angle $\theta = \left(0.74^{+0.16}_{-0.11}\right)^{\circ}$[10]. The data for HS2 can be found in Supplementary Note 2. As shown there, it is worth remarking that for HS2, featuring greater $\theta$ than HS1, longer decay times $\tau_{d,n}$ are found. This is in accordance with the larger momentum mismatch between the charge pair of the moiré exciton in HS2 and agrees with the results presented in ref. 6.

The different states of the moiré potential also exhibit a different formation dynamics. Figure 2c shows the time evolution of the MX signal in HS1 up to 1 ns after the laser pulse excitation. In this case, the data are reproduced by

$$I_{rise}(t) = -A_r \cdot \exp\left(-\frac{t - t_0}{\tau_r}\right) + I_{decay}(t) \quad (2)$$

where $\tau_r$ is the luminescence rise time and $I_{decay}$ represents the decay part of the data. By fitting the decay part first, the data in the (0-1) ns time interval can be reproduced by Eq. 2, with only $A_r$ and $\tau_r$ as fitting parameters. The $\tau_r$ values are displayed in panel c of Fig. 2 (the data corresponding to the high-energy range, shown in the right-most panel, are close to the resolution limit and could not be fitted reliably). The data indicate that the highest-energy excited state of the moiré

https://doi.org/10.1038/s41467-024-44739-9

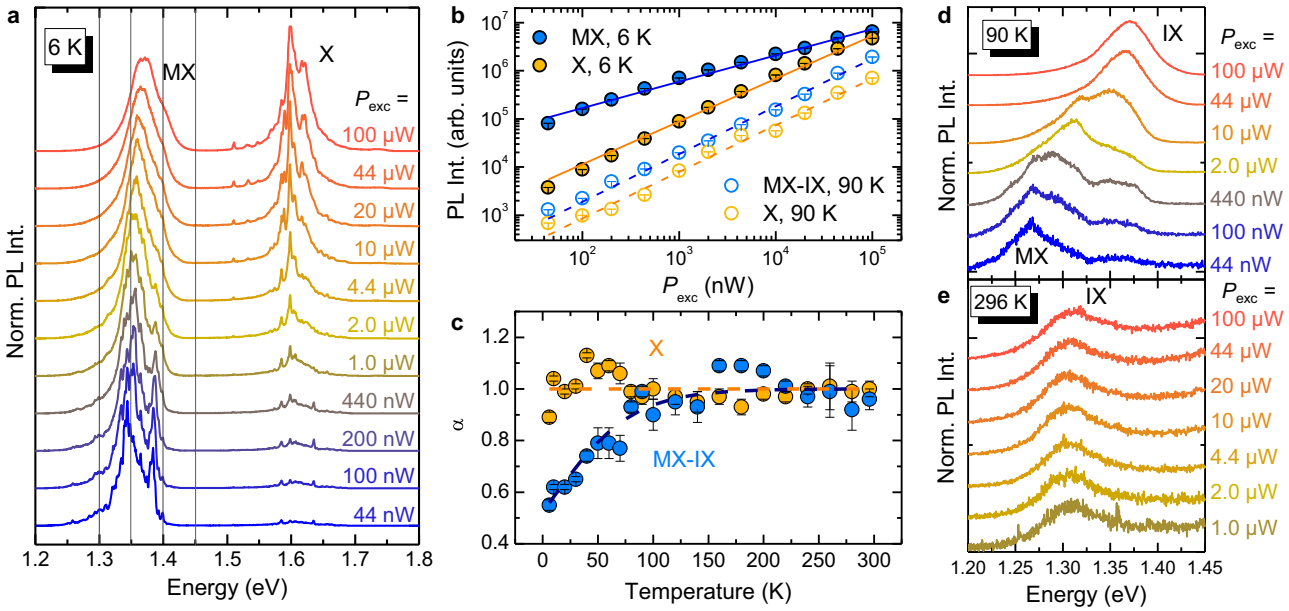


**Fig. 3 | Photo-generated carrier density and temperature dependence of the exciton bands. a** $T = 6$ K $\mu$-PL spectra of HS1 recorded for different laser excitation power values. MX indicates the moiré exciton band and X the intralayer exciton recombination in the $MoSe_2$ and $WSe_2$ layers (lower- and higher-energy side, respectively). **b** PL integrated intensity dependence on the laser power $P_{exc}$ for the MX or MX-IX bands (azure symbols) and for the X band (light orange symbols) at $T = 6$ K (full symbols) and $T = 90$ K (open symbols), respectively. Solid and dashed lines are fits to the data with Eq. (3) for $T = 6$ K and 90 K, respectively. At $T$=6 K, the $\alpha$ coefficient values are $0.55 \pm 0.02$ and $0.89 \pm 0.02$ for MX and X, respectively. At $T = 90$ K, the $\alpha$ coefficient values are $0.99 \pm 0.02$ and $0.97 \pm 0.03$ for MX-IX and X, respectively. **c** Temperature variation of the $\alpha$ coefficient for the MX-IX and X bands. In the former case, a clear transition from a sublinear to a linear behaviour is found and ascribed to the transition from a moiré localisation regime to a free interlayer exciton one (hence the mixed label MX-IX). **d** $T = 90$ K $\mu$-PL spectra for different laser excitation powers in the energy region where the MX and IX recombinations can be simultaneously observed. IX takes over MX upon increase of the photo-generated carrier density. **e** Same as **d** for $T = 296$ K, where only the IX transition is observable.

potential (together with the likely population of moiré excitons in the relative minimum at the $R_h^h$ registry) is populated faster (<100 ps), similar to what reported in ref. 19. Instead, the population of the lowest-energy state requires more time to reach its quasi-equilibrium occupancy because of the extra contribution from higher-energy levels in addition to the direct excitation. Power-dependent tr-$\mu$-PL measurements on both HSs, reported in Supplementary Note 4 and 5, show a progressive shortening of the time decay of the MX band as $P_{exc}$ increases. This is a likely consequence of exciton-exciton interactions, that tend to diminish the exciton lifetime[35,36].

## Exciton recombination vs carrier density and temperature

The X and MX recombination bands also exhibit quite distinct spectral behaviours when the density of photo-generated excitons and the lattice temperature are increased. Figure 3a shows the cw $\mu$-PL spectra of HS1 at $T = 6$ K for $P_{exc}$ ranging from 44 nW (i.e. 5.6 W/cm$^2$) to 100 $\mu$W (i.e. $1.3 \cdot 10^4$ W/cm$^2$). The MX band broadens and its centroid blueshifts with increasing $P_{exc}$, likely as a consequence of the dipole-dipole interaction between MXs[5,13,22,26,37,38]. Following Ref. 13, we determine that in the $P_{exc}$ = (0.044-100) $\mu$W range the density of photo-generated electron-hole pairs within the HS varies from $n_{e\text{-}h} = 1.1 \cdot 10^{11}$ cm$^{-2}$ to $2.3 \cdot 10^{13}$ cm$^{-2}$ (see Supplementary Note 4). We note that the highest $n_{e\text{-}h}$ achieved by us is smaller than the value necessary to observe an optically induced Mott transition from IXs to spatially separated electron and hole gases[13]. Nevertheless, from the previously estimated period of the moiré potential $a_m = 40$ nm, the corresponding density of moiré minima is equal to $7.2 \cdot 10^{10}$ cm$^{-2}$ and a sizeable exciton-exciton interaction is possible thus explaining the decrease in the emission decay time reported in Supplementary Note 4 and 5 as well as the MX band blueshift with $P_{exc}$[13,22,38]. Recent simulations based on the Green's function formalism[38] showed that exciton densities around $10^{11} - 10^{12}$ cm$^{-2}$ trigger intercell hopping and exciton delocalisation effects, which reflect in a blue-shift and broadening of the moiré emission band. In the present case, we observe such effects starting from $P_{exc} = 4.4$ $\mu$W (see Fig. 3b), corresponding to $n_{e\text{-}h} \approx 4 \cdot 10^{12}$ cm$^{-2}$, in good agreement with ref. 38. On the other hand, the X band, which, as we recall, comprises the $MoSe_2$ and $WSe_2$ intralayer excitons, does not change appreciably its centroid. It instead gains significant spectral weight compared to MX, which originates from recombination centres with finite spatial density. Figure 3b shows the dependence of the integrated intensity $I$ of the HS exciton and X bands as a function of $P_{exc}$ for $T = 6$ K and $T = 90$ K. At 90 K, the HS exciton band is labelled MX-IX to indicate the contribution from IXs (or de-trapped MXs) occurring at high $P_{exc}$ and increasing temperature, as we are going to demonstrate. The integrated intensity was obtained by performing integrals over suitable energy ranges (it cannot be reliably obtained by fitting the data since the shape of the PL bands changes with power, comprising the appearance of narrow lines at low power). The data were fitted by:

$$I = A \cdot P_{exc}^{\alpha}, \quad (3)$$

where $A$ is a scaling constant. At $T = 6$ K, $\alpha$ is equal to $0.55 \pm 0.02$ for MX and $0.89 \pm 0.02$ for X. The smaller $\alpha$ found at low $T$ for the MX signal from the HS (as opposed to that from intralayer excitons X in the MLs) is compatible with the finite number of energy states available for excitons trapped in the quantised levels of the moiré potential minima. Furthermore, the localised nature of MXs can lead to enhanced exciton-exciton interactions that act as a probable source of signal loss. Instead, the nearly linear behaviour of the X emission intensity is consistent with the virtually unlimited number of intralayer excitons that can be photo-generated. Interestingly, Fig. 3b shows that the nearly linear dependence of the X band on $P_{exc}$ is maintained also at $T = 90$ K, while a major variation is found for the MX-IX band that can be explained by considering an increasingly higher spectral contribution of free IXs at higher $T$. As a matter of fact, the $\alpha$ value of MX-IX becomes approximately equal to 1 at 90 K.

Puzzled by this finding, we investigated the dependencies on $P_{exc}$ of the integrated area of the MX-IX and X bands at different temperatures. The full set of power-dependent data can be found in Supplementary Note 6. Figure 3c summarises the variation of the coefficient $\alpha$ with $T$, as obtained from Eq. (3). For the X band, a nearly linear behaviour is observed at all temperatures. Instead, for the MX-IX band, $\alpha$ increases progressively from 0.55 to about 1 as $T$ is increased from 5 K to 120 K, with a linear behaviour observed at higher temperatures, up to room temperature. These results suggest a qualitative change in the nature of the exciton-related bands in the HS at about 120 K. A similarly comprehensive study was performed also for HS2, which has a larger twist angle of 0.74°. The results are shown in Supplementary Note 7. As for HS1, the X band shows a linear behavior ($\alpha$ = 1) all over the temperature range. Although also in HS2 the coefficient $\alpha$ for the MX-IX band exhibits a progressive increase from 0.5 to 1 (see Supplementary Note 7), the plateau-value of 1 is reached at a temperature of about 100 K (lower than the 120 K value observed in HS1; see Fig. 3c) consistently with the shallower moiré potential at greater twist angles[39]. On the one hand, these results strengthen the picture described so far. On the other hand, they point to the crucial role of the twist angle in determining the thermal stability of moiré excitons and associated phenomena in moiré superlattices.

Figures 3d and e display a series of spectra recorded on HS1 at different $P_{exc}$ for $T$ = 90 K and $T$ = 296 K, respectively. In the first case, the lineshape of the MX band changes significantly as the density of photoexcited carriers increases. Indeed, we notice a considerable spectral weight transfer by about 100 meV from the structured band around 1.27 eV (at the lowest $P_{exc}$) to the single component peaked at about 1.37 eV (at the highest $P_{exc}$). We ascribe this change to the saturation of moiré-localised excitons in favour of moiré-de-trapped IXs (the related 100 meV band shift is indeed close to the moiré potential depth for R-type $WSe_2/MoSe_2$ HS[3,4,7]). This behaviour is not evident at the lowest $T$ values (see, e.g., Fig. 3a), when MXs are frozen in their potential minima. Eventually, for $T$ > 200 K, almost all MXs are ionised and only IXs are observed, as shown in Fig. 3e, clearly demonstrating the absence of a sizeable lineshape variation with $P_{exc}$. See Supplementary Note 7 for similar data recorded on HS2 (having greater $\theta$).

### Moiré exciton de-trapping, magnetic moment and dynamics vs $T$

The moiré exciton de-trapping is even more evident in Fig. 4a, which shows the $\mu$-PL spectra of HS1 for different $T$ values and $P_{exc}$ = 10 $\mu$W; similar studies for higher and lower $P_{exc}$ are shown in Supplementary Note 8. From $T$ = 6 K to $T$ = 120 K, the HS signal is dominated by the MX band, which undergoes a redistribution of the carrier population between the different states of the moiré potential. Starting from $T$ = 120 K, a high-energy component due to IXs appears and becomes increasingly important relative to the MX band, until the latter vanishes at about 220 K. Finally, at room temperature only IXs are visible. At $T \approx 160$ K, the two contributions coexist so that their energy difference can be estimated. The obtained value, equal to about 90 meV, fits well with the exciton barrier height of the moiré potential in R-type $WSe_2/MoSe_2$ HSs[3,4,7], where only the exciton singlet state is optically permitted (the MX-IX energy distance becomes 75 meV in the HS2 with greater $\theta$). Although qualitatively, also this observation agrees with the expected shallower moiré potential depth for greater twist angles[39]; see Supplementary Notes 6 and 7). In contrast, the exciton ground state in H-type HSs is in a triplet configuration, with the singlet state having an energy 25 meV higher[5,22,27]. Also, we exclude that the two transitions coexisting at intermediate $T$ are ascribable to $K_{CB}$-$K_{VB}$ (CB and VB stand for conduction and valence band, respectively) and $\Lambda_{CB}$-$K_{VB}$ IX transitions[21], which differ by 55 meV[21].

It is worth mentioning that different results were reported in the literature. In ref. 28, the MX de-trapping was observed by monitoring the PL intensity and lifetime of $WSe_2/MoSe_2$ HSs with a transition temperature < 50 K that is in contrast with our results. On the other hand, exciton diffusivity measurements[7] showed the absence of MX de-trapping in a $WSe_2/MoSe_2$ HS with nearly perfect lattice alignment ($\theta$ = 0.15°), while a clear de-trapping was visible for $\theta$ > 2°[7].

In any case, the here observed temperature-induced change in the nature of the exciton in the HS should be reflected in the electronic properties of the levels involved in the excitonic transition. In this respect, the exciton magnetic moment and the associated gyromagnetic factor $g_{exc}$ −embedding the spin, orbital and valley properties of the bands− turned out to be an extremely sensitive parameter of the electronic structure of nanostructures[40] and of 2D crystals[41–44] and their HSs[5,10,20,22–24,26,45–48]. In $WSe_2/MoSe_2$ HSs, the lowest-energy exciton state is in a spin-singlet configuration for R-type HSs and in a spin-triplet configuration for H-type HSs[49]. The spin-singlet and spin-triplet excitons feature a $g_{exc}$ value with a positive (≈+ 7) and a negative (≈−15) sign, respectively, the exact value depending on the specific sample[5,20,22,24,25,46–48]. Our HS is R-type, as discussed before, and therefore we expect a positive $g_{exc}$ value. Figure 4b shows the magnetic field, $B$, dependent $\mu$-PL spectra of HS1 in the HS exciton region at $T$ = 10 K and $P_{exc}$ = 10 nW (corresponding to $n_{e\text{-}h} = 2.0 \cdot 10^{10}$ cm$^{-2}$, see Supplementary Note 4). For each field, the opposite circular polarisations $\sigma^{\pm}$ were recorded simultaneously on two different regions of the CCD detector, see Methods. Figure 4b shows the $\sigma^+$ and $\sigma^-$-polarised $\mu$-PL spectra that exhibit several narrow lines due to different MXs. They all undergo a Zeeman splitting (ZS) given by

$$ZS(B) = E^{\sigma^+} - E^{\sigma^-} = g_{exc} \cdot \mu_B B. \quad (4)$$

$E^{\sigma^{\pm}}$ are the peak energies of components with opposite helicity $\sigma^+$ and $\sigma^-$, and $\mu_B$ is the Bohr magneton. The positive (negative) energy shift with $B$ of the $\sigma^+$ ($\sigma^-$) component of the lines displayed in Fig. 4b indicates that $g_{exc} > 0$ for the individual MXs. Then, magneto-$\mu$-PL measurements were performed also at $T$ = 160 K and $P_{exc}$=75 $\mu$W, where the HS exciton band is instead dominated by free IXs. Figure 4c shows the $\sigma^+$ and $\sigma^-$ components of the IX spectra at different magnetic fields. Remarkably, the two components shift with $B$ accordingly to a negative ZS, i.e. opposite to that found at $T$ = 10 K for the MX lines (for IXs, the $\sigma^+$ red component is at lower energy than the $\sigma^-$ blue one). Figure 4d shows the ZS field dependence for the MX lines at 10 K and for the IX band at 160 K, both fitted by Eq. (4). The resulting $g_{exc}$ for the (trapped) MXs and (free) IXs are $g_{exc,MX} = +6.73 \pm 0.10$ (this is an average value over the 5 measured MXs) and $g_{exc,IX} = -4.64 \pm 0.10$, respectively. The former is in close agreement with previous experimental[5,23,46,47] and theoretical[20] results found for MXs in R-type $WSe_2/MoSe_2$ HSs. As reported in Supplementary Note 9, we performed similar measurements and found similar results for HS2. For HS1, we also derived the ZS of the five gaussians into which the moiré exciton band can be deconvolved at low $T$ and $P_{exc}$, as shown in Fig. 1c. As discussed in Supplementary Note 10, in comparison to the single MX lines of Fig. 4d, a smaller ZS is found for the Gaussian components, resulting in an average $g_{exc} = +4.43 \pm 0.89$. The smaller $g_{exc}$ for the Gaussian components might be caused by exciton-exciton interactions. In fact, the Gaussian lineshape could be the consequence not only of a distribution of an ensemble of single moiré lines, but also of an exciton interaction-induced broadening of the the moiré emission itself. As for the results at 160 K, to our knowledge there are no previous ZS measurements on HSs at high temperatures. We found a similar negative $g_{exc,IX}$ value of about −5 also at $T$ = 210 K and 100 K, as described in Supplementary Note 11. The origin of the sign reversal of $g_{exc,IX}$ must be then ascribed to the avoided effect of the moiré potential caused by the temperature-induced de-trapping of the MXs. As a matter of fact, we can estimate $g_{exc,IX}$ considering the separate contribution of electrons and holes to the IX gyromagnetic factor, as usually done for excitons in semiconductors. Following an analogous

https://doi.org/10.1038/s41467-024-44739-9

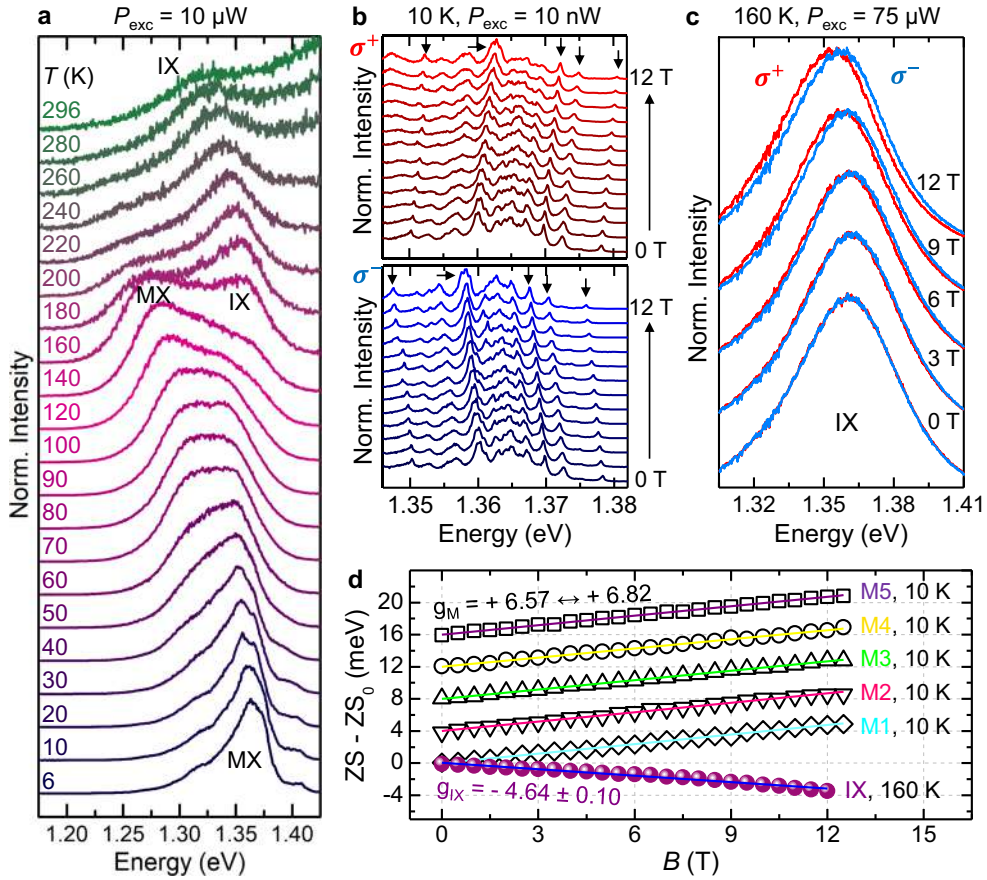


**Fig. 4 | Exciton magnetic moment sign reversal. a** $\mu$-PL spectra of HS1 recorded for different temperatures and fixed $P_{exc}$ = 10 $\mu$W focused via a 20 × objective (NA=0.4). MX indicates the moiré exciton band and IX the free interlayer exciton recombination. Note the major spectral transfer from MXs to IXs for $T$ > 120 K. **b** Magneto-$\mu$-PL spectra from 0 to 12 T (in steps of 1 T) of the MX band at $T$ = 10 K and $P_{exc}$ = 10 nW (focused via a 100× objective with NA = 0.82). The upper and lower panels correspond to the $\sigma^+$ (red) and $\sigma^-$ (blue) circular polarisations, respectively. The data are stacked by y-offset. The positive and negative slopes of the $\sigma^+$ and $\sigma^-$ polarisations with the field indicate a positive gyromagnetic factor. The arrows denote some specific MX lines. **c** Magneto- $\mu$-PL spectra at $T$ = 160 K and $P_{exc}$ = 75 $\mu$W of the free IX band for the $\sigma^+$ and $\sigma^-$ polarisations. A negative Zeeman splitting (ZS) can be observed, with the $\sigma^+$ and $\sigma^-$ spectra being at lower and higher energy, respectively. **d** ZS of the five moiré-localised excitons M1 to M5 highlighted by the arrows in panel **b** (M1 is the lowest energy one, M5 the highest) and of the free IX exciton vs magnetic field measured in panel **c**, resulting in the gyromagnetic factors displayed in the figure. The ZS data of the M2 to M5 lines were shifted by y-offset for ease of visualisation. Error bars are within the symbol size.

procedure to that employed in ref. 43 for strained $WS_2$ MLs, for this HS we use

$$g_{exc,IX} = 2\left[L_{CB}(MoSe_2) - L_{VB}(WSe_2)\right], \quad (5)$$

where the first and second terms are the expectation values of the orbital angular momentum of the $MoSe_2$ CB and $WSe_2$ VB, respectively (the spin contribution cancels out because the band extrema involved in the free IX transition have the same spin for R-type HSs). As reported in ref. 20, $L_{CB}(MoSe_2)$ = 1.78 and $L_{VB}(WSe_2)$ = 4.00 and from Eq. (5) we obtain $g_{exc,IX}$ = − 4.44 in very good agreement with the value we found experimentally for the free IX transition shown in Fig. 4d. To this regard, it is relevant to add that a positive $g_{exc}$ is found for the MX band also at $T$ = 80 K, as shown by $\mu$-PL measurements on HS1 performed at $B$ = 16 T and sufficiently low laser power (as low as 10 nW) to emphasize the contribution of the MX band at high $T$; see Supplementary Note 11.

Interestingly, the suppression of the moiré potential in an R-type $WSe_2/MoSe_2$ HS caused by inserting a h-BN layer between the constituent MLs leads to magneto-PL results similar to ours[50]. Indeed, in Ref. 50 the spatial decoupling between the HS single MLs determines a sign reversal and a decrease of the $g_{exc}$ modulus analogous to that found here by increasing the lattice temperature.

The exciton ZS in $WSe_2/MoSe_2$ HSs may depend on the local atomic registry, too[20]. Figure 5a shows a series of $\mu$-PL spectra recorded on HS1 with opposite circular polarisation ($\sigma^+$ and $\sigma^-$) at different magnetic fields for $T$ = 6 K and low laser excitation power $P_{exc}$ = 0.2 $\mu$W. Several narrow lines due to moiré confined excitons can be observed, superimposed on a continuum background. Like in Fig. 4b, the MX lines exhibit a positive Zeeman splitting with average $g_{exc,MX}$ = + 6.78 ± 0.11 (panel c of the figure). Figure 5b shows the same study of panel a recorded on the same point of the HS but with a $P_{exc}$ value increased by about a factor of 400. The narrow lines associated to moiré confined excitons merge forming a single band, whose maximum shows a blue-shift of more than 30 meV with respect to the low-energy side of the MX band at lower $P_{exc}$. Quite interestingly and unexpectedly, under these circumstances, the ZS value reverses its sign resulting in a gyromagnetic factor $g_{exc}$ = − 6.93, as shown in Fig. 5c. We also performed a PL study at fixed $B$ = 16 T by varying $P_{exc}$ over more than three orders of magnitude. The data are described in Supplementary Note 12 for both HS1 and HS2 and show how when increasing the density of excitons the initially positive ZS due to the single moiré excitons eventually goes negative as the MX component broadens and blue-shifts. To interpret these results we note that: (i) the $P_{exc}$-induced blue-shift is significantly smaller than 100 meV (i.e., the moiré potential depth[3,4,7]) and (ii) the modulus of $g_{exc}$ (|−6.93|) found at high $P_{exc}$ and $T$ = 10 K is larger than that (| − 4.64|)

https://doi.org/10.1038/s41467-024-44739-9

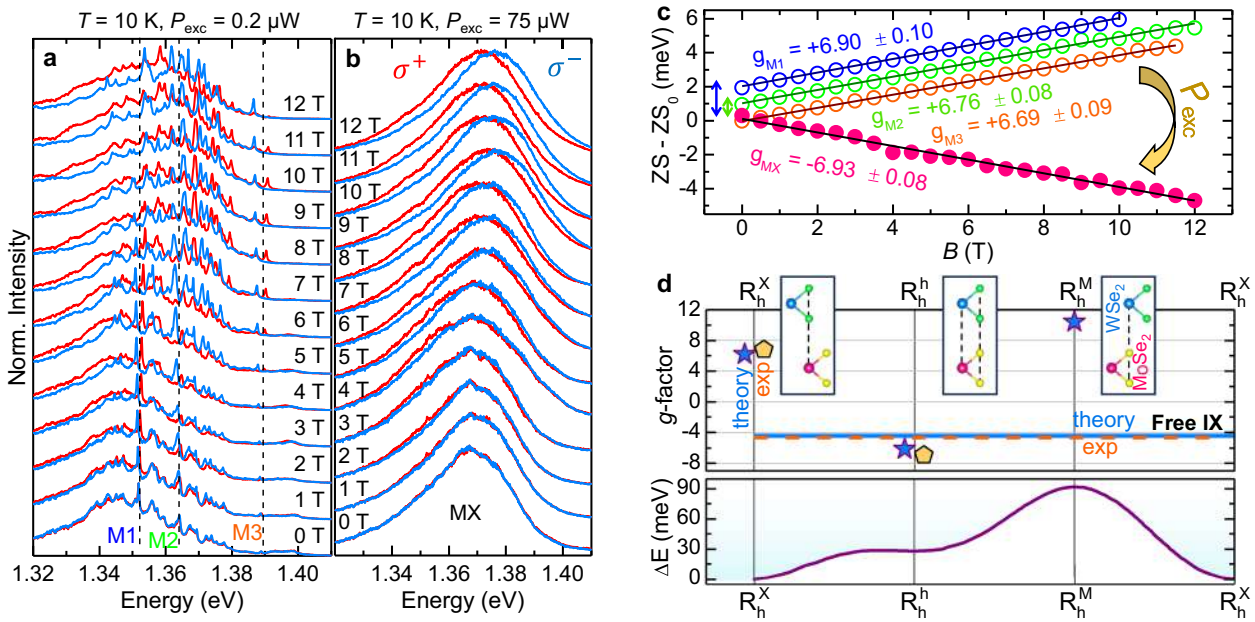


**Fig. 5 | Unveling the moiré atomic registry through *g*-factor measurements.** **a**, **b** Helicity-resolved normalised $\mu$-PL spectra of HS1 under magnetic field at $T = 6$ K for two different laser excitation powers $P_{exc}$ (focused via a 100 × objective with NA = 0.82). The two sets of data were acquired in the same point of the HS. For $P_{exc} = 0.2$ $\mu$W (**a**), many narrow lines can be seen. M1, M2 and M3 indicate three such narrow lines. At high powers $P_{exc} = 75$ $\mu$W (**b**) a continuous band can be seen. **c** ZS of the lines M1-M3 of panel **a** and of the MX band of panel **b**, showing an opposite sign of the *g*-factor. The data of lines M2 and M3 are up-shifted by 1 and 2 meV, respectively (as indicated by the double-sided arrows on the left) for sake of clarity. **d** Top: Theoretical *g*-factors (cyan stars) estimated for MXs confined in the $R_h^X$, $R_h^h$, and $R_h^M$ atomic registries[20]. The experimental *g*-factors calculated for the MX lines at low power (as an average of the *g*-factors estimated for the M1, M2 and M3 lines of panel **c**), and for the MX band measured at high power (pink data in panel **c**) are displayed as orange pentagons, and −based on their value− are associated to the $R_h^X$ and $R_h^h$ registries, respectively. The cyan solid line and the orange dashed line provide the *g*-factor calculated based on Eq. (5) and that measured experimentally (Fig. 4c, d) for the free IX, respectively. The insets show the atomic alignment corresponding to the three atomic registries. Error bars are within the symbol/line size. Bottom: Variation of the interlayer exciton potential landscape with respect to its minimum at the $R_h^X$ point (ΔE) in R-type $MoSe_2/WSe_2$ HSs. Adapted from the calculations of ref. 3.

measured at high $T$ (see Fig. 4c, d), where moiré de-trapped (and thus free) excitons (IXs) dominate the emission spectrum. Thus, we conclude that the main contribution to the MX band in Fig. 5b (high $P_{exc}$) comes from moiré excitons with $R_h^h$ local registry. Indeed, at low power, the lowest energy $R_h^X$ states are first populated. When $P_{exc}$ is increased, the $R_h^h$ states, that lie just a few tens of meV at higher energy (see Fig. 5d), start to be populated and, for sufficiently high power, dominate the emission spectrum. The $R_h^M$ states, that lie at even higher energy, are not visible due to their small oscillator strength[20]. This picture is corroborated by theoretical calculations, showing that $g_{exc} = +6.19$ for the $R_h^X$ registry, while $g_{exc} = -6.15$ for the $R_h^h$ registry[20]. Figure 5d summarises these findings and provide a comparison between experimental and theoretical $g_{exc}$ values for moiré-localised as well as free IX excitons. The quantitative potential landscape for the moiré potential is also shown, as derived from ref. 3.

These results demonstrate how magnetic fields represent a valuable tool to determine the localised or delocalised status of charge carriers in 2D HSs, which can be important for the understanding of fundamental effects, such as the formation of highly correlated electronic phases[12,13,16,51].

The sign reversal of the *g*-factor upon temperature increase is accompanied by a change in the MX formation and recombination dynamics when the de-trapping process starts to occur with increasing $T$. Figure 6a displays the time evolution of the $\mu$-PL exciton signal in HS1 within 1 ns after the laser excitation, which corresponds predominantly to the exciton formation process. Different temperatures were considered with $P_{exc} = 44$ nW ($n_{e\text{-}h}$=1.1 · $10^{11}$ cm$^{-2}$).

It is clear that the MX formation dynamics becomes faster with increasing $T$ (for $T \leq 100$ K and $P_{exc} = 44$ nW, MXs dominate). The experimental data were fitted by Eq. (2) and the $T$ dependence of $\tau_r$ is displayed in panel **b** for two different photo-generated carrier densities. At $T = 100$ K, $\tau_r$ approaches the temporal resolution limit (notice that once the data get close to the resolution limit, the estimated rise time is affected by the system response and thus only qualitatively indicative). The higher temperatures and the ensuing MX ionisation process result indeed in a decreased contribution of the moiré localisation step, and thus in a reduction of the time required to build up the exciton population contributing to the MX/IX band. This process is more evident with increasing $P_{exc}$, as can be noted in Fig. 6b. As a matter of fact, a larger photo-generated carrier density tends to saturate the MX states shifting the spectral centroid of the MX-IX band towards the faster-forming IX levels.

The luminescence decay is also highly influenced by temperature variations. Figure 6c shows the MX-IX band decay curves at $P_{exc}$ = 1 $\mu$W ($n_{e\text{-}h} = 1.2 \cdot 10^{12}$ cm$^{-2}$) and different temperatures. The curves can be reproduced using Eq. (1) and the values of the fitting parameters ($\tau_{d,n}$ and $w_{d,n}$) are displayed in Fig. 6d. The three values of the decay time $\tau_{d,n}$ decrease monotonically, with the shorter one ($\tau_{d,1}$) reaching the resolution limit (0.23 ns) at $T = 140$ K, and the weights of the slower components ($w_{d,2}$ and $w_{d,3}$) becoming less important. The latter are particularly relevant at low $T$, where decay time values of about 200 ns are observed, consistent with the space-indirect nature of MXs. The, yet small, k-space mismatch associated with the twist angle may also contribute to the lengthening of the luminescence decay time[6]. The marked decrease of $\tau_{d,n}$ with $T$ can be explained by two simultaneous mechanisms. First, non-radiative recombination channels are activated at higher temperatures, greatly shortening the luminescence decay time. Second, delocalised states are expected to have a larger recombination probability, because they are more likely to interact with other oppositely charged free carriers, or with lattice defects acting as non-radiative channels[52].

https://doi.org/10.1038/s41467-024-44739-9

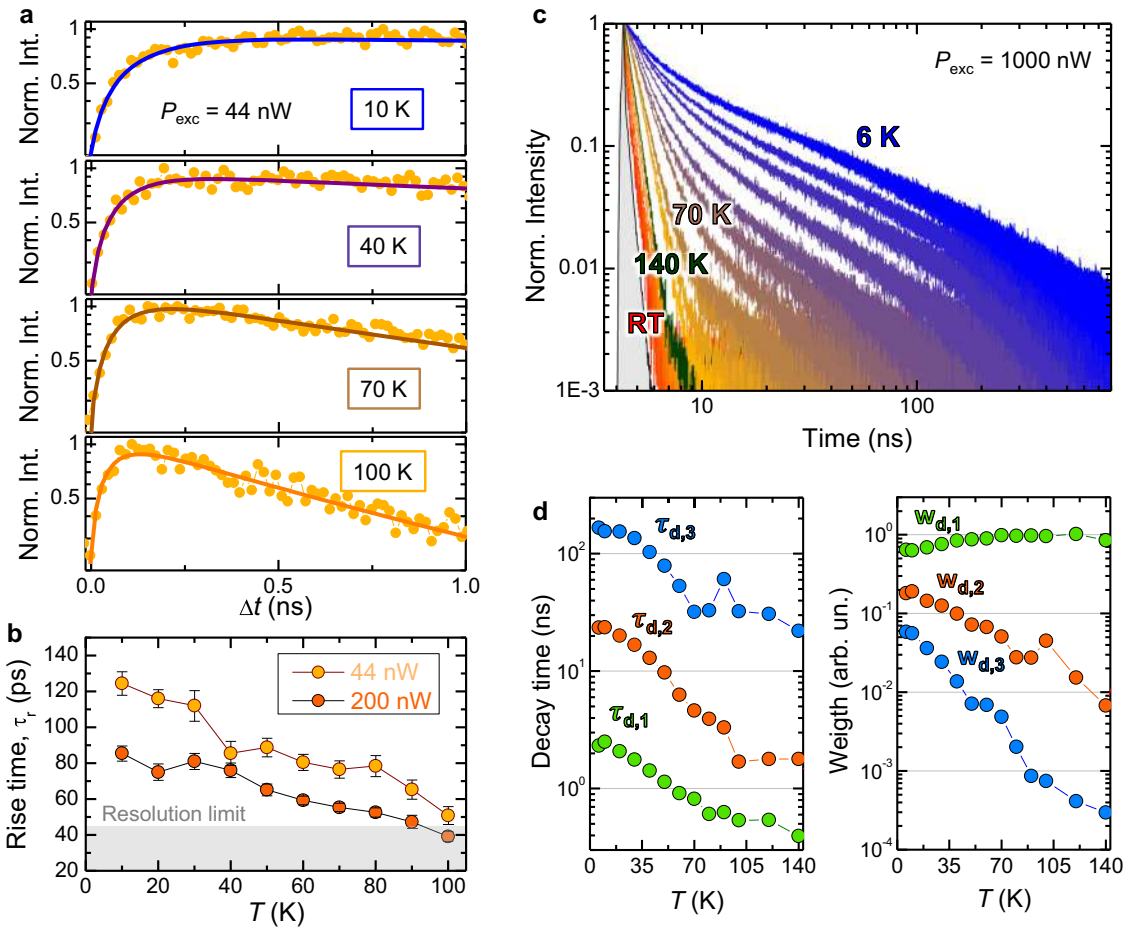


**Fig. 6 | Rise and decay times with increasing temperature. a** Time-evolution of the $\mu$-PL signal of the investigated $WSe_2/MoSe_2$ heterostructure (HS1) recorded at different temperatures (and fixed laser excitation power $P_{exc}$ = 44 nW) in the Δt = 0 − 1.0 ns interval from the laser pulse. The detection energy was set at the MX-IX band (see Fig. 3). The solid lines are fits to the data by Eq. (2). **b** Rise time $\tau_r$ values obtained by fitting the experimental data for different temperatures and two $P_{exc}$ values. The setup time resolution is shown by the grey area. Notice that once the data get close to the resolution limit, the estimated rise time is affected by the system response and thus only qualitatively indicative. **c** Time-evolution of the $\mu$-PL signal of the MX-IX band (see Fig. 3) recorded in the Δt = 0-800 ns interval from the laser pulse. The data were recorded at different temperatures, as indicated in the figure, and fixed $P_{exc}$. The grey area indicates the instrumental response. **d** Decay times $\tau_{d,n}$ values used to reproduce the data of panel **c** via Eq. (1). The same for the spectral weights $w_{d,n}$ of the different time components, see Eq. (1).

In summary, we investigated the process of temperature-induced exciton de-trapping from moiré minima in $WSe_2/MoSe_2$ HSs. We observed that at temperatures above 100 K moiré excitons turn into free interlayer excitons with relevant consequences for quantum technology applications[11] and for the observation of many-body phenomena, such as exciton condensation[12] or Mott transition[13,16,51]. The temperature-induced transition from a moiré-confined to a free IX regime manifests itself in a sizeable variation of the power law governing the exciton signal growth with photo-generated carrier density. The exciton magnetic moment too undergoes major variations with increasing $T$. Indeed, the interlayer exciton $g$-factor exhibits a remarkable reversal of its sign and decrease of its modulus (going from about +7 to about −5) concomitantly with the de-trapping of the moiré-confined excitons for $T \gtrsim 100$ K. This is likely to have relevant consequences for valleytronic applications of TMD HSs. Within the same $T$ interval, we also consistently found that the formation time of MXs is strongly reduced, as a consequence of the cross-over from a localised to a free-like regime. This indicates that the exciton capture in the moiré potential requires an intermediate step that lengthens the luminescence rise time. Also, the decay time of the MX/IX states is greatly reduced by increasing $T$ due to the increased recombination probability of freely moving excitons as well as to exciton-exciton interactions and to thermally activated non-radiative recombination channels. Our findings shed new light on the truly confined nature of the exciton states in a moiré superlattice with increasing temperature and exciton density, thus setting the conditions for the observation and stability of highly correlated phases at elevated temperatures in moiré superlattices.

## Methods

### Sample fabrication

The HSs were fabricated by the standard dry transfer technique. TMD flakes were mechanically exfoliated by the scotch tape method and deposited on PDMS. $MoSe_2$ and $WSe_2$ MLs on the PDMS were identified and deposited. For HS1, the $MoSe_2$ ML was deposited first on a $SiO_2$/Si substrate, and the $WSe_2$ was deposited atop of it. h-BN flakes were then exfoliated with the same approach and a thin h-BN flake was identified on the PDMS. The flake was then deposited in such a way to cap the HS completely. The twist angle between the MLs was then estimated by SHG measurements. For HS2, a h-BN flake was first deposited on a $SiO_2$/Si substrate. The $WSe_2$ ML was then deposited atop. The orientation of the ML was checked by SHG. The orientation of the $MoSe_2$ ML on PDMS was also checked, and the ML was deposited aligned to the $WSe_2$ ML (virtually null twist angle). This HS was also subsequently capped with a thin h-BN flake. The twist angle of the two HSs was then determined more precisely by optical studies (see Supplementary Note 2).

After every deposition step, the samples were annealed in high vacuum at 150 °C for some hours.

### Continuous-wave $\mu$-PL measurements

For $\mu$-PL measurements, the excitation laser was provided by a single frequency Nd:$YVO_4$ lasers (DPSS series by Lasos) emitting at 532 nm. The luminescence signal was spectrally dispersed by a 20.3 cm focal length Isoplane 160 monochromator (Princeton Instruments) equipped with a 150 grooves/mm and a 300 grooves/mm grating and detected by a back-illuminated $N_2$-cooled Si CCD camera (100BRX by Princeton Instruments). The laser light was filtered out by a very sharp long-pass Razor edge filter (Semrock). A 100 × long-working-distance Zeiss objective with NA = 0.75 was employed to excite and collect the light, in a backscattering configuration using a confocal setup.

For high resolution measurements aimed at higlighting the moiré energy levels (Fig. 1c and Supplementary Fig. 2.1), a 75 cm focal length Acton monochromator was used.

### Time-resolved $\mu$-PL measurements

For tr $\mu$-PL measurements, the sample was excited with a ps supercontinuum laser (NKT Photonics) tuned at 530 nm, with a full width at half maximum of about 10 nm and 50 ps pulses at 1.2 MHz repetition rate. The sample was excited in the same experimental configuration used for continuous wave measurements. The signal was then collected in a backscattering configuration using a confocal setup. The desired spectral region was selected by using longpass and shortpass filters. The signal was thus focused by means of a lens on an avalanche photodetector from MPD with temporal resolution of 30 ps.

### $\mu$-PL excitation measurements

For $\mu$-PL excitation ($\mu$-PLE), we employed the same ps supercontinuum laser used for tr $\mu$-PL. The laser wavelength was automatically changed by an acousto-optic tunable filter and employing a series of shortpass and longpass filters to remove spurious signals from the laser. The detection wavelength was selected using the same monochromator and detector employed for cw $\mu$-PL measurements.

### Magneto-$\mu$-PL measurements

Magneto-$\mu$-PL measurements were performed at variable temperature in a superconducting magnet reaching up to 16 T. x-y-z piezoelectric stages were used to excite the sample and collect the signal from the desired point of the sample. A 515-nm-laser and a 100 × microscope objective with NA = 0.82 were used. The same objective was used to collect the luminescence. The circular polarisation of the PL was analysed using a quarter-wave plate (that maps circular polarisations of opposite helicity into opposite linear polarisations) and a Wollaston prism steering the components of opposite linear polarisation (and thus of opposite helicity) to different lines of the liquid-nitrogen-cooled Si-CCD we employed (100BRX by Princeton Instruments). In this manner, the $\sigma^+$ and $\sigma^-$ components could be measured simultaneously. A monochromator with 0.75 m focal length (Princeton Instruments) and a 600 grooves/mm grating was used to disperse the PL signal.

### Second harmonic generation measurements

The measurements were performed by using the 900 nm line of a tunable pulsed Ti:Sapphire laser with a pulse width of <100 fs and a repetition rate of 80 MHz. The sample was excited and measured under a 50 × confocal objective lens (NA = 0.85), and the frequency-duplicated light was collected in a backscattering configuration. Linear polarisers were used to select laser light and SHG signal with given polarisation states. The sample was placed on a rotation stage to collect the SH response in terms of relative polarisation angles.

## Data availability

The data that support the findings of this study are available from the corresponding authors upon request.

## References


1. Lau, C. N., Bockrath, M. W., Mak, K. F. & Zhang, F. Reproducibility in the fabrication and physics of moiré materials. *Nature* **602**, 41 (2022).
2. Zhang, C. et al. Interlayer couplings, moiré patterns, and 2D electronic superlattices in $MoS_2/WSe_2$ hetero-bilayers. *Sci. Adv.* **3**, e1601459 (2017).
3. Yu, H., Liu, G.-B., Tang, J., Xu, X. & Yao, W. Moiré excitons: From programmable quantum emitter arrays to spin-orbit-coupled artificial lattice. *Sci. Adv.* **3**, e1701696 (2017).
4. Tran, K. et al. Evidence for moiré excitons in van der Waals heterostructures. *Nature* **567**, 71 (2019).
5. Seyler, K. L. et al. Signatures of moiré-trapped valley excitons in $MoSe_2/WSe_2$ heterobilayers. *Nature* **567**, 66 (2019).
6. Choi, J. et al. Twist angle-dependent interlayer exciton lifetimes in van der Waals heterostructures. *Phys. Rev. Lett.* **126**, 047401 (2021).
7. Li, Z. et al. Interlayer exciton transport in $MoSe_2/WSe_2$ heterostructures. *ACS Nano* **15**, 1539 (2021).
8. Du, L. et al. Moiré photonics and optoelectronics. *Science* **379**, eadg0014 (2023).
9. Zhang, N. et al. Moiré intralayer excitons in a $MoSe_2/MoS_2$ heterostructure. *Nano Lett.* **18**, 7651 (2018).
10. Liu, E. et al. Signatures of moiré trions in $MoSe_2/WSe_2$ heterobilayers. *Nature* **594**, 46 (2021).
11. Baek, H. et al. Highly energy-tunable quantum light from moiré-trapped excitons. *Sci. Adv.* **6**, eaba8526 (2020).
12. Wang, Z. et al. Evidence of high-temperature exciton condensation in two-dimensional atomic double layers. *Nature* **574**, 76 (2019).
13. Wang, J. et al. Optical generation of high carrier densities in 2D semiconductor heterobilayers. *Sci. Adv.* **5**, eaax0145 (2019).
14. Huang, D., Choi, J., Shih, C.-K. & Li, X. Excitons in semiconductor moiré superlattices. *Nat. Nanotechnol.* **17**, 227 (2022).
15. Chen, D. et al. Excitonic insulator in a heterojunction moiré superlattice. *Nat. Phys.* **18**, 1171 (2022).
16. Regan, E. C. et al. Mott and generalized Wigner crystal states in $WSe_2/WS_2$ moiré superlattices. *Nature* **579**, 359 (2020).
17. Xu, Y. et al. Correlated insulating states at fractional fillings of moiré superlattices. *Nature* **587**, 214 (2020).
18. Wu, F., Lovorn, T. & MacDonald, A. H. Theory of optical absorption by interlayer excitons in transition metal dichalcogenide heterobilayers. *Phys. Rev. B* **97**, 035306 (2018).
19. Tan, Q., Rasmita, A., Zhang, Z., Novoselov, K. S. & Gao, W.-B. Optical signature of cascade transitions between moiré interlayer excitons. *Phys. Rev. Lett.* **129**, 247401 (2022).
20. Woźniak, T., Junior, P. E. F., Seifert, G., Chaves, A. & Kunstmann, J. Exciton *g* factors of van der Waals heterostructures from first-principles calculations. *Phys. Rev. B* **100**, 235408 (2020).
21. Barré, E. et al. Optical absorption of interlayer excitons in transition-metal dichalcogenide heterostructures. *Science* **376**, 406 (2022).
22. Brotons-Gisbert, M. et al. Moiré-trapped interlayer trions in a charge-tunable $WSe_2/MoSe_2$ heterobilayer. *Phys. Rev. X* **11**, 031033 (2021).
23. Li, W., Lu, X., Dubey, S., Devenica, L. & Srivastava, A. Dipolar interactions between localized interlayer excitons in van der Waals heterostructures. *Nat. Mater.* **19**, 624 (2020).
24. Nagler, P. et al. Giant magnetic splitting inducing near-unity valley polarization in van der Waals heterostructures. *Nat. Commun.* **8**, 1551 (2017).
25. Wang, T. et al. Giant valley-Zeeman splitting from spin-singlet and spin-triplet interlayer excitons in $WSe_2/MoSe_2$ heterostructure. *Nano Lett.* **20**, 694 (2020).

26. Li, W., Lu, X., Wu, J. & Srivastava, A. Optical control of the valley Zeeman effect through many-exciton interactions. *Nat. Nanotechnol.* **16**, 148 (2021).
27. Zhang, L. et al. Highly valley-polarized singlet and triplet interlayer excitons in van der Waals heterostructure. *Phys. Rev. B* **100**, 041402(R) (2019).
28. Mahdikhanysarvejahany, F. et al. Temperature dependent moiré trapping of interlayer excitons in $MoSe_2$-$WSe_2$ heterostructures. *npj 2D Mater. Appl.* **5**, 67 (2021).
29. Miller, B. et al. Long-lived direct and indirect interlayer excitons in van der Waals heterostructures. *Nano Lett.* **17**, 5229 (2017).
30. Troue, M. et al. Extended spatial coherence of interlayer excitons in $MoSe_2$/$WSe_2$ heterobilayers. *Phys. Rev. Lett.* **131**, 036902 (2023).
31. Parzefall, P. et al. Moiré phonons in twisted $MoSe_2$-$WSe_2$ heterobilayers and their correlation with interlayer excitons. *2D Mater.* **8**, 035030 (2021).
32. Shinokita, K., Watanabe, K., Taniguchi, T. & Matsuda, K. Valley relaxation of the moiré excitons in a $WSe_2$/$MoSe_2$ heterobilayer. *Nano Lett.* **22**, 16862 (2022).
33. Robert, C. et al. Exciton radiative lifetime in transition metal dichalcogenide monolayers. *Phys. Rev. B* **93**, 205423 (2016).
34. Blundo, E. et al. Evidence of the direct-to-indirect band gap transition in strained two-dimensional $WS_2$ and $MoS_2$, and $WSe_2$. *Phys. Rev. Res.* **2**, 012024 (2020).
35. Aivazian, G. et al. Many-body effects in nonlinear optical responses of 2D layered semiconductors. *2D Mater.* **4**, 025024 (2017).
36. Salehzadeh, O., Tran, N. H., Liu, X., Shih, I. & Mi, Z. Exciton kinetics, quantum efficiency, and efficiency droop of monolayer $MoS_2$ light-emitting devices. *Nano Lett.* **14**, 4125 (2014).
37. Nagler, P. et al. Interlayer exciton dynamics in a dichalcogenide monolayer heterostructure. *2D Mater.* **4**, 025112 (2017).
38. Brem, S. & Malic, E. Bosonic delocalization of dipolar moiré excitons. *Nano Lett.* **23**, 4627 (2023).
39. Lin, B.-H. et al. Remarkably deep moiré potential for intralayer excitons in $MoSe_2$/$MoS_2$ twisted heterobilayers. *Nano Lett.* **23**, 1306 (2023).
40. Tedeschi, D. et al. Unusual spin properties of inp wurtzite nanowires revealed by Zeeman splitting spectroscopy. *Phys. Rev. B* **99**, 161204(R) (2019).
41. Stier, A. V. et al. Magnetooptics of exciton Rydberg states in a monolayer semiconductor. *Phys. Rev. Lett.* **120**, 057405 (2018).
42. Molas, M. R. et al. Probing and manipulating valley coherence of dark excitons in monolayer $WSe_2$. *Phys. Rev. Lett.* **123**, 096803 (2019).
43. Blundo, E. et al. Strain-induced exciton hybridization in $WS_2$ monolayers unveiled by Zeeman-splitting measurements. *Phys. Rev. Lett.* **129**, 067402 (2022).
44. Olkowska-Pucko, K. et al. Excitons and trions in WSSe monolayers. *2D Mater.* **10**, 015018 (2023).
45. Gobato, Y. G. et al. Distinctive *g*-factor of moiré-confined excitons in van der Waals heterostructures. *Nano Lett.* **22**, 8641 (2022).
46. Ciarrocchi, A. et al. Polarization switching and electrical control of interlayer excitons in two-dimensional van der Waals heterostructures. *Nat. Photon.* **13**, 131 (2019).
47. Joe, A. Y. et al. Electrically controlled emission from singlet and triplet exciton species in atomically thin light-emitting diodes. *Phys. Rev. B* **103**, L161411 (2021).
48. Holler, J. et al. Interlayer exciton valley polarization dynamics in large magnetic fields. *Phys. Rev. B* **105**, 085303 (2022).
49. Yu, H., Liu, G.-B. & Yao, W. Brightened spin-triplet interlayer excitons and optical selection rules in van der Waals heterobilayers. *2D Mater.* **5**, 035021 (2018).
50. Mahdikhanysarvejahany, F. et al. Localized interlayer excitons in $MoSe_2$/$WSe_2$ heterostructures without a moiré potential. *Nat. Commun.* **13**, 5354 (2022).
51. Tang, Y. et al. Simulation of Hubbard model physics in $WSe_2$/$WS_2$ moiré superlattices. *Nature* **579**, 353 (2020).
52. Vinattieri, A. et al. Role of the host matrix in the carrier recombination of InGaAsN alloys. *Appl. Phys. Lett.* **82**, 2805 (2003).


## Acknowledgements

The authors thank Andrey Chaves, Paulo E. Faria Jr and Tomasz Woźniak for useful discussions about the magneto-photoluminescence results and are grateful to Daniele Sanvitto for support with the SHG measurements. E.B., A.P., A.B., and M.R.M. acknowledge support by the European Union's Horizon 2020 research and innovation programme through the ISABEL project (No. 871106). This project was funded within the QuantERA II Programme that has received funding from the European Union's Horizon 2020 research and innovation programme under Grant Agreement No. 101017733, and with funding organisations Ministero dell'Università e della Ricerca (A.P. and M.F.) and by Consiglio Nazionale delle Ricerche (G.P.). A.P. and M.F. acknowledge financial support from the PNRR MUR project PE0000023-NQSTI. M.F. and G.P. acknowledge funding from the PRIN2022 project DELIGHT2D (Prot. 20222HNMYE). E.B. acknowledges support from La Sapienza through the grants Avvio alla Ricerca 2021 (Grant no. AR12117A8A090764) and Avvio alla Ricerca 2022 (Grant no. AR2221816B672C03). The authors acknowledge support from the National Science Centre, Poland, through Grants No. 2018/31/B/ST3/02111 (K.O. P. and M.R.M.) and No. 2017/27/B/ST3/00205 (A.B.). K.W. and T.T. acknowledge support from the JSPS KAKENHI (Grant Numbers 19H05790 and 20H00354).

## Author contributions

E.B. and A.P. conceived and supervised the research. E.B. and M.C. fabricated the heterostructures. E.B., F.T., S.C., M.C. and G.C. performed the optical measurements and analysed the data. E.B., A.P., K.O.P., L.K., and M.R.M. performed the magneto-optical measurements, with the support of A.B., and E.B. analysed the data. A.M. provided support for the SHG measurements. M.F. provided support for the time-resolved measurements. G.P. contributed to the sample characterisation. T.T. and K.W. grew the hBN samples. E.B. and A.P. wrote the manuscript. The results and the manuscript were approved by all the coauthors.

## Competing interests

The authors declare no competing interests.

## Additional information

**Supplementary information** The online version contains supplementary material available at https://doi.org/10.1038/s41467-024-44739-9.

**Correspondence** and requests for materials should be addressed to Elena Blundo or Antonio Polimeni.

**Peer review information** *Nature Communications* thanks Xiaoxu Zhao, Fateme Mahdikhany and the other anonymous reviewer for their contribution to the peer review of this work. A peer review file is available.

SUPPLEMENTARY INFORMATION for

# Localisation-to-delocalisation transition of moiré excitons in $WSe_2/MoSe_2$ heterostructures

Elena Blundo,[1,*] Federico Tuzi,[1] Salvatore Cianci,[1] Marzia Cuccu,[1] Katarzyna Olkowska-Pucko,[2] Łucja Kipczak,[2] Giorgio Contestabile,[1] Antonio Miriametro,[1] Marco Felici,[1] Giorgio Pettinari,[3] Takashi Taniguchi,[4] Kenji Watanabe,[5] Adam Babiński,[2] Maciej R. Molas,[2] and Antonio Polimeni[1,*]

[1] *Physics Department, Sapienza University of Rome, 00185, Roma, Italy.*
[2] *Institute of Experimental Physics, Faculty of Physics, University of Warsaw, Pasteura 5, 02-093 Warsaw, Poland*
[3] *Institute for Photonics and Nanotechnologies (CNR-IFN), National Research Council, 00133, Rome, Italy*
[4] *International Center for Materials Nanoarchitectonics, National Institute for Materials Science, 1-1 Namiki, Tsukuba 305-0044, Japan.*
[5] *Research Center for Functional Materials, National Institute for Materials Science, 1-1 Namiki, Tsukuba 305-0044, Japan*

[*] Corresponding authors: elena.blundo@uniroma1.it, antonio.polimeni@uniroma1.it

## Contents

# Supplementary Note 1. Micro-photoluminescence spectra of HS1 and HS2 before and after hBN-capping

Fig. 1.1 shows a comparison between the $\mu$-PL spectra of both HS1 and HS2 acquired at 6 K and with the same power both before and after capping with h-BN. Indeed, a shift of the MX band can be noticed for HS1 after capping, while no significant difference can be noticed for HS2. It should also be noticed that the MX band is very close in energy for HS1 (after capping) and HS2.

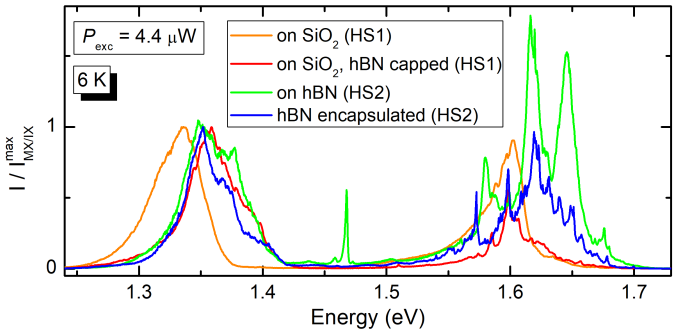


**Figure 1.1:** $\mu$-PL spectra acquired at 6 K and with analogous power on HS1 (deposited on a $SiO_2$ substrate) and on HS2 (deposited on a hBN flake) before and after hBN-capping.

The energy of our MX band ($E_{\mathrm{PL}}$) agrees with those reported in the literature. Figure 1.2(a) shows the PL peak energies of $WSe_2/MoSe_2$ HSs with the corresponding reference. All data refer to low temperature ($T$<20 K) PL measurements and all HSs were encapsulated by h-BN (but papers indicated as g, k and q in the figure legend). We grouped the data into two sets depending

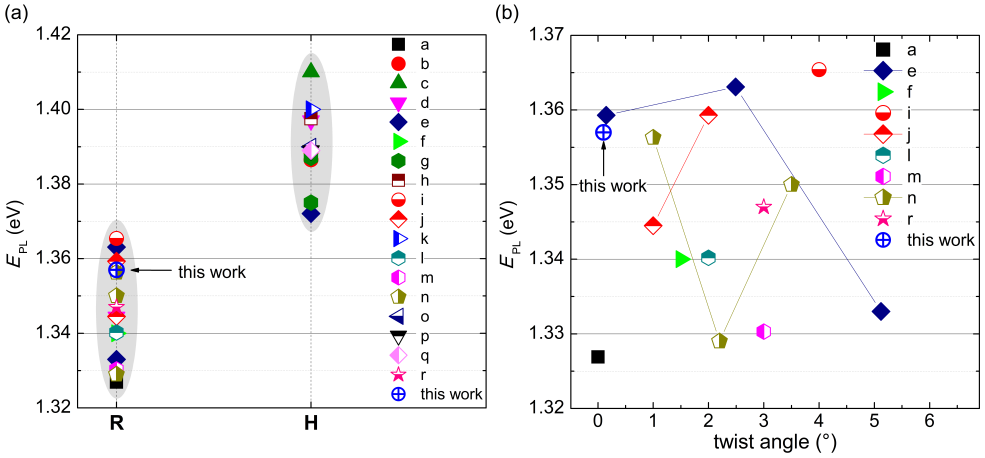


**Figure 1.2:** (a) Survey of the photoluminescence (PL) peak energies, $E_{\mathrm{PL}}$, of $WSe_2/MoSe_2$ HSs as reported in the literature. R and H indicate HSs with twist angle $\theta \approx 0°$ and $\theta \approx 60°$, respectively. (b) Same data as in (a) for R-type HSs as a function of $\theta$. The plot shows only data for which the twist angle is provided by the authors. References. a:[1]; b:[2]; c:[3]; d:[4]; e:[5]; f:[6]; g:[7]; h:[8]; i:[9]; j:[10]; k:[11]; l:[12]; m:[13]; n:[14]; o:[15]; p:[16]; q:[17]; r:[18].

on the relative alignment angle: *i*) R-type HSs corresponding to a twist angle, $\theta$, around 0° and *ii*) H-type HSs corresponding to $\theta$ around 60°. We note that the $E_{\mathrm{PL}}$ values relative to each type of HS remain rather distinct, although a large spread of values is observed within each type of HS. Fig. 1.2(b) shows the dependence on $\theta$ of $E_{\mathrm{PL}}$ for R-type HSs (namely, the type investigated

in our work). The plot includes $E_{\mathrm{PL}}$ values for those works, where $\theta$ was given. Clearly, no well-defined trend can be overall observed. This is likely due to the large uncertainties in the determination of $\theta$, local deviations from a regular structure caused by imperfections and local strains accompanied by important atomic level reconstruction that result in a non-ideal/regular moiré potential [19]. The R-type HSs considered in our work feature $E_{\mathrm{PL}}$ values, which are higher than the average reported values, yet well within the literature distribution of $E_{\mathrm{PL}}$ for R-type HSs (see Fig. 1.2).

As for our HSs, we tested their homogeneity by scanning the laser across their surface.

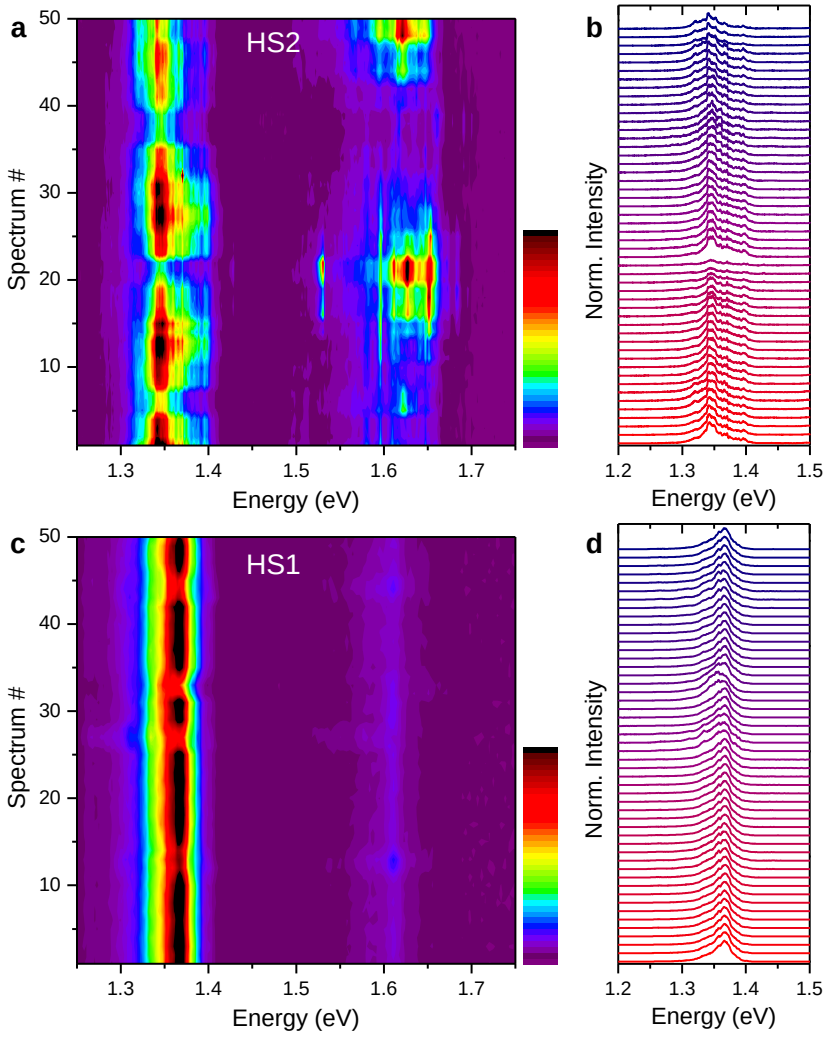


**Figure 1.3:** **a-b** Colour plot (**a**) and normalised stacked spectra (**b**) of the $\mu$-PL measurements performed while scanning the laser ($P_{\mathrm{exc}} = 0.22\ \mu$W) over HS2 with an S-like scan. The scanning step was of about 0.3 $\mu$m. **c-d** Same for HS1. The drops in the intensity of the MX (and corresponding enhancement of the intralayer excitons signal), which can be noticed especially for HS2, are due to the fact that the HS edge was reached. Apart from such drops, the intensity and lineshape of the MX is pretty uniform.

Fig. 1.3 shows such a study performed on both HS2 and HS1. The measurements were taken by performing an S-scan on the central part of each HS, with steps of about 0.3 $\mu$m. The intensity drops revealed by the colour plots are due to the fact that the scan reached the edge of the HS. Overall, both HSs show a very good degree of homogeneity as far as the resonance energy distances and relative spectral weight are concerned. A bit larger degree of fluctuation is instead observed regarding the emission intensity.

Overall, the central part of the HSs is pretty uniform, and some variations can be noticed only towards the edges. Our study reveals that the sample homogeneity is indeed such that the results discussed in our work hold a general validity and are not related to some specific spots in the sample.

## Supplementary Note 2. Moiré period and stacking angle

The Hamiltonian for excitons confined in a moiré potential can be described as [20, 10]:

$$H = \hbar\Omega_0 + \frac{\hbar^2 k^2}{2M} + \Delta(\mathbf{r}), \tag{2.1}$$

where the first term is an energy constant, the second term is the center of mass kinetic energy, $M$ is the exciton mass and $\Delta(\mathbf{r})$ is the moiré potential energy. For a $MoSe_2/WSe_2$ HS, $M \approx 0.84 m_e$, where $m_e$ is the electron bare mass [10]. Near its minima, the moiré potential $\Delta(\mathbf{r})$ can be approximated as parabolic: $\Delta(\mathbf{r}) = \beta(\mathbf{r}/a_M)^2/2$, where $a_M$ is the moiré potential period and $\beta$ is a constant independent of $a_M$. Excitons confined in this parabolic potential have quantised energy levels:

$$E_m = \sqrt{\frac{\beta\hbar^2}{M a_M^2}} \cdot (n_x + n_y + 1), \tag{2.2}$$

where $n_{x,y}$ are non-negative integers [20]. The spacing between subsequent levels is thus:

$$S = \sqrt{\frac{\beta\hbar^2}{M a_M^2}}. \tag{2.3}$$

Following ref. [10], $\beta = 2.84$ eV.

The moiré period $a_M$ can thus be estimated by measuring the spacing, as:

$$a_M = \frac{1}{S} \cdot \sqrt{\frac{\beta\hbar^2}{M}}. \tag{2.4}$$

For our HSs, we thus acquired low power (5 nW) spectra at 6 K with higher spectral resolution (we used a monochromator with a focal length of 75 cm), as shown in Fig. 2.1, and fitted the spectra with 5 gaussians. The number of gaussians was established empirically, in order to reproduce the spectra reliably but to avoid exceeding with their number (and thus with the fitting parameters). We performed the fitting without imposing strict conditions on the spacing, and determined the average spacing for both HS1 and HS2 as: $S_{\mathrm{HS1}} = (12.8 \pm 1.3)$ meV and $S_{\mathrm{HS2}} = (20.3 \pm 3.4)$ meV. Through Eq. 2.4, we estimate: $a_{M,\mathrm{HS1}} = (39.8 \pm 3.9)$ nm and $a_{M,\mathrm{HS2}} = (25.1 \pm 4.2)$ nm. According to the calculations by Liu *et al.* [2], such periods correspond to stacking angles of $\theta_{\mathrm{HS1}} = (0.46^{+0.05}_{-0.04})^\circ$ and $\theta_{\mathrm{HS2}} = (0.74^{+0.16}_{-0.11})^\circ$.

Indeed, these angles are both very close to zero. For HS2, the fabrication process was made based on the crystal orientation derived by second harmonic generation (SHG) measurements. The HS was fabricated with a virtually null twist angle, but the uncertainty in the SHG data and those in the fabrication process itself entail an uncertainty of about a couple degrees in the fabrication process. The estimated angle $\theta_{\mathrm{HS2}} \approx 0.74^\circ$ is thus in good agreement with the expected null angle. For HS1, instead, the fabrication process was not based on SHG measurements. We thus performed SHG *a posteriori* to verify the crystal orientation. The results are displayed in Fig. 2.2.

The SHG measurements were performed while keeping the polarisation of the detected signal and that of the excitation laser fixed and parallel. The sample was then rotated by an angle $\theta$ with respect to an arbitrary set of laboratory coordinates (X,Y). Fig. 2.2 displays the SHG measurements taken on pieces of the $WSe_2$ and $MoSe_2$ MLs that stick out of the HS. The two sets of data were then fitted by the equation:

$$I_{\mathrm{SHG}} = \left[A \cdot \cos\left(3\theta'\right)\right]^2, \quad \theta' = \theta - \theta_0 \tag{2.5}$$

where $\theta'$ is the angle between the excitation laser polarisation and the armchair direction, and $\theta_0$ defines the direction of the armchair lattice direction with respect to the X axis of the laboratory

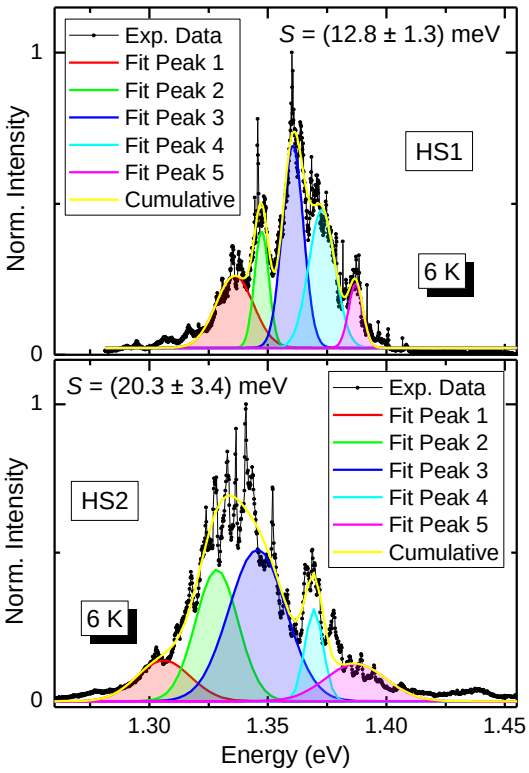


**Figure 2.1:** $\mu$-PL spectra of the MX band acquired with very low laser power excitation (5 nW). The spectrum can be reproduced by five Gaussian functions that are spaced on average by (12.8±1.3) meV (the individual spacings are 11.4, 13.2, 12.2, 14.3 meV) for HS1, and by (20.3 ± 3.4) meV (the individual spacings are 22.5, 17.1, 23.8, 17.6 meV) for HS2. The very narrow lines that make up the broader Gaussian peaks correspond to single MXs recombining in moiré minima.

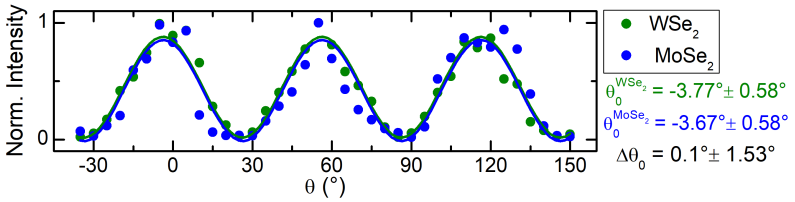


**Figure 2.2:** SHG normalised intensity measured in the $WSe_2$ and $MoSe_2$ MLs that constitute HS1 as a function of the rotation angle of the sample.

system. Indeed, the $\theta_0$ angles found for $WSe_2$ and $MoSe_2$ are very close to each other, with a relative twist $\Delta\theta_0 = 0.1° \pm 1.53°$. This confirms that our HS is characterised by a very small twist angle close to zero, in agreement with the results obtained by the analysis of the spacing between the enregy levels of the moiré band.

Finally, we also performed a comparative study between the decay times of the PL signal of the two HSs. Indeed, Choi et al. [14] showed how the decay time of MX/IX is sensitive to the twist angle, and in particular increases dramatically while going from a twist of 1° to 3°, a feature related to the larger k-space mismatch for larger twist angles. Indeed, as shown in Fig.2.3 , HS2 exhibits exciton PL decay times longer than those observed in HS1 as expected based on the slightly larger twist angle of HS2 with respect to HS1.

Our results agree very well with those reported in Ref. [14] for a $MoSe_2/WSe_2$ HS with a 1° twist angle, for which a 21 meV spacing was found between the energy levels (thus very close to what we found for HS2). In that work, the time-resolved measurements concerning the HS with

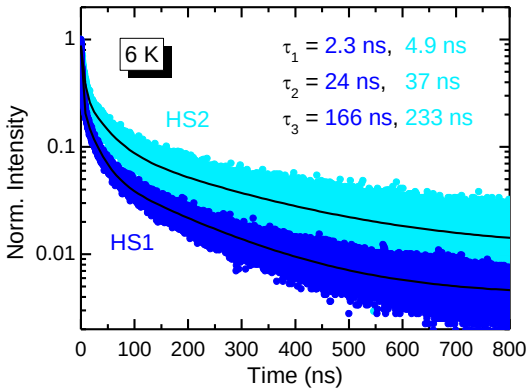


**Figure 2.3:** Time-evolution of the $\mu$-PL signal of HS2 recorded in the $\Delta$t=0-800 ns interval from the laser pulse and comparison with the analogous data acquired for HS1. The excitation power was 1 $\mu$W. The data were fitted by Eq. 1 of the main text, and the estimated decay times are displayed, showing how larger decay times are found for HS2 compared to HS1.

a 1° twist angle were collected only in the (0-25) ns range from the laser pulse and were fitted by a double exponential function providing decay times of 1-2 ns and 6-10 ns. If we restrict our data to the same time range of (0-25) ns and fit them with a double exponential, we get decay times of about 2 and 11 ns for HS2, which indeed agree well with those by Choi et al. [14]. This discussion highlights however the importance of acquiring and analysing the time-resolved data on an appropriate range, since when restricting the data to a relatively short range the result is possibly much more affected by the presence of non-radiative decay channels and the slow dynamics that characterises MXs cannot be fully appreciated.

## Supplementary Note 3. Time-resolved micro-photoluminescence data

Fig. 3.1 shows the time resolved $\mu$-PL data of Fig. 2 of the main text, displayed on a suitable time scale in order to compare them with the laser pulse data. Indeed, the data concerning the

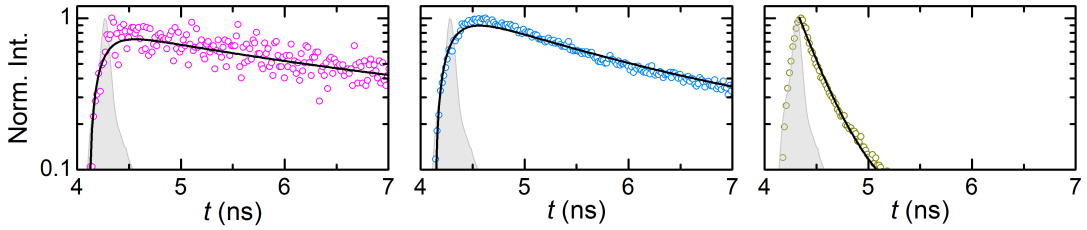


**Figure 3.1:** Time-evolution of the $\mu$-PL signal and laser pulse (light grey) on the three spectral regions highlighted in Fig. 2**a** of the main text. The data are the same of Figs. 2**b-c** of the main text, but plotted in the first few ns of acquisition in order to enable a comparison with the laser curve.

low (pink) and middle (cyan) energy ranges, show a much slower rise and decay dynamics if compared to the laser pulse. For the high energy range, instead, the decay part gets faster (but still longer than the resolution limit), while the rise part of the data is clearly resolution limited (in fact, as discussed in the main text, the rise time cannot be derived).

By fitting the decay part of the data in Fig. 2**b** of the main text, we obtained the fitting weights and decay times displayed in the following table.

**Table 3.1:** Fitting parameter values obtained by fitting the data in Fig. 2**b** by Eq. (1) of the main text. $\tau_{d,n}$ is the decay time relative to the $n$-th component, whose weight is given by $w_{d,n}$.

| Energy Range | $\tau_{d,1}$ (ns) | $w_{d,1}$ (%) | $\tau_{d,2}$ (ns) | $w_{d,2}$ (%) | $\tau_{d,3}$ (ns) | $w_{d,3}$ (%) |
|---|---|---|---|---|---|---|
| Low (pink) | $2.27 \pm 0.09$ | $60.9 \pm 1.4$ | $14.0 \pm 0.6$ | $34.6 \pm 0.8$ | $51 \pm 4$ | $4.4 \pm 0.7$ |
| Medium (cyan) | $1.59 \pm 0.01$ | $78.1 \pm 0.4$ | $15.2 \pm 0.2$ | $15.8 \pm 0.1$ | $77.0 \pm 0.3$ | $6.0 \pm 0.1$ |
| High (yellow) | $< 0.23$ | $86.0 \pm 0.4$ | $1.03 \pm 0.01$ | $13.0 \pm 0.3$ | $13.5 \pm 0.1$ | $1.0 \pm 0.1$ |

## Supplementary Note 4. Estimation of photogenerated carrier density

Figure 3 in the main text shows the cw $\mu$-photoluminescence (PL) spectra at $T$=6 K varying the laser power $P_{\rm exc}$ between 44 nW and 100 $\mu$W. To each $P_{\rm exc}$ value we associate a specific density of electron-hole pairs $n_{\rm e-h}$ photogenerated within the HS. This was done following Ref. [9]. Below we summarise the procedure followed.

Under continuous wave (cw) excitation, the generation rate of photogenerated carriers is given by

$$G(n_{\rm e-h}) = \frac{P_{\rm exc} \cdot \sigma(n_{\rm e-h})}{S \cdot h\nu}, \tag{4.1}$$

where $\sigma(n_{\rm e-h})$ is the dependence of the absorbance of the $MoSe_2/WSe_2$ HS on the photogenerated carrier density, $S = \pi r^2$ is the laser spot area with $r$=500 nm, and h$\nu$=2.33 eV is the exciting photon energy. In addition, in a stationary (*i.e.* continuous wave) regime we have

$$\frac{{\rm d}n_{\rm e-h}}{{\rm d}t} = G(n_{\rm e-h}) - \frac{n_{\rm e-h}}{\tau(n_{\rm e-h})} = 0, \tag{4.2}$$

where $\tau(n_{\rm e-h})$ is the dependence of the exciton decay time of the $MoSe_2/WSe_2$ HS on the photogenerated carrier density. To solve this equation we need to derive $\sigma(n_{\rm e-h})$ and $\tau(n_{\rm e-h})$.

$\sigma(n_{\rm e-h})$ was previously reported in Ref. [9] and it is reproduced in Fig. 4.1.

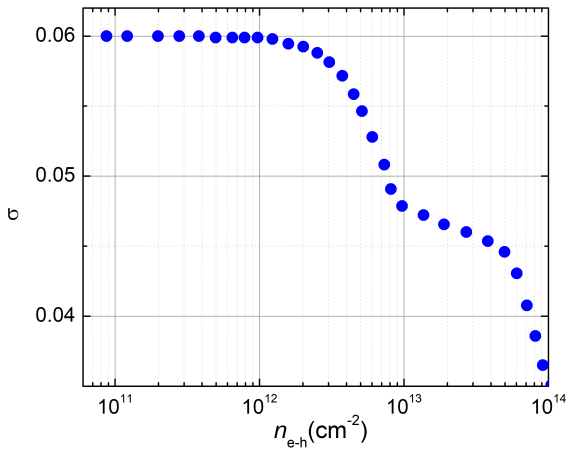


**Figure 4.1:** Optical absorbance of a $MoSe_2/WSe_2$ HS as a function of the density of photogenerated carriers for photon energy equal to 2.33 eV. The data were taken from Fig. 4 of Ref. [9].

$\tau(n_{\rm e-h})$ was deduced in two steps. We first measured the time decay of the exciton $\mu$-PL signal, whose temporal traces are shown in Fig. 4.2 for different $P_{\rm exc}$s. We then fitted the data using Eq. (1) in the main text with $n = 3$ components characterised by their decay time $\tau_{\rm d,n}$ with relative weight $w_{\rm d,n}$. Table 4.1 reports the $\tau_{\rm d,n}$ and $w_{\rm d,n}$ values for different $P_{\rm exc}$s along with the weighted value of the decay time $\tau$. Finally, we obtained $\tau(n_{\rm e-h})$ using the following relationship under pulsed excitation between the injected carrier density $n$ and $P_{\rm exc}$:

$$n = \frac{P_{\rm exc} \cdot \sigma}{S \cdot f_{\rm rep} \cdot h\nu}, \tag{4.3}$$

where $\sigma$=0.08 is the absorbance of the $MoSe_2/WSe_2$ HS evaluated for h$\nu$=2.33 eV as reported in Ref. [9] of this Supplementary Material, and $f_{\rm rep}$=1.2 MHz is the pulsed laser repetition rate. Therefore, we can relate $n$ to $P_{\rm exc}$ and hence to $\tau$ via Table 4.1. Fig. 4.3 shows the dependence of $\tau$ on $n$.

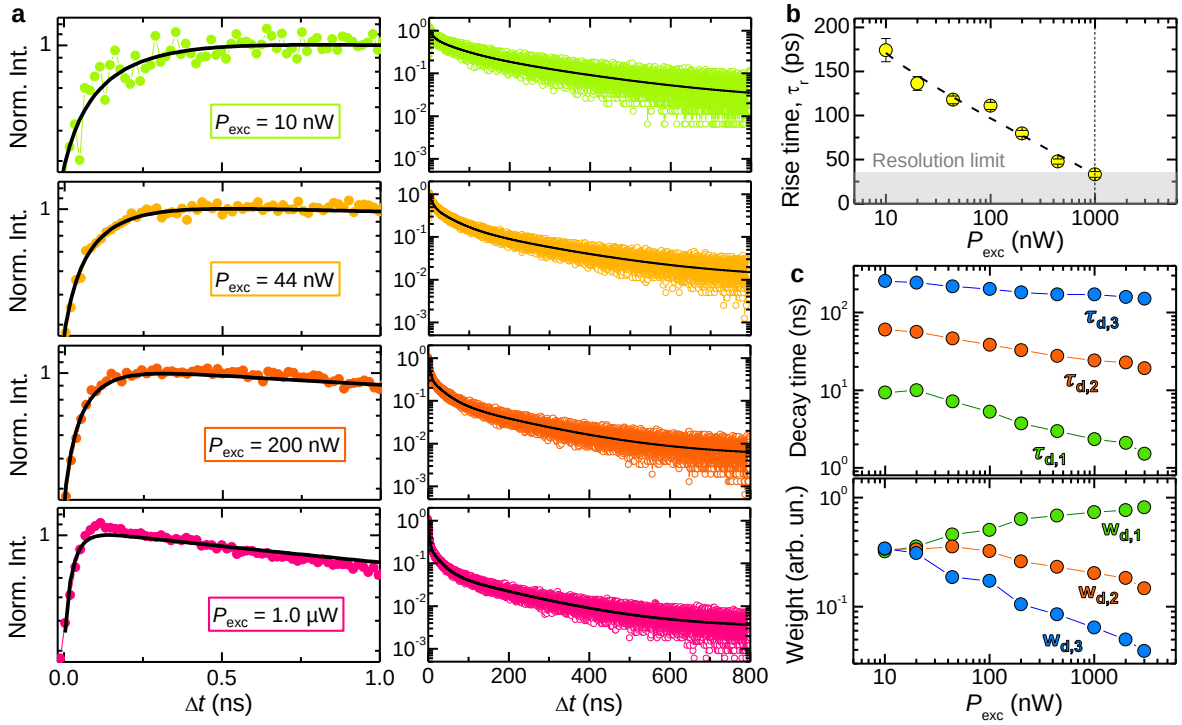


**Figure 4.2:** **a** Some exemplifying plots of the time-evolution of the $\mu$-PL signal of the investigated $WSe_2/MoSe_2$ HS recorded at 6 K for different excitation powers $P_{exc}$, in the $\Delta t$=0-800 ns interval from the laser pulse. The detection energy was set at the MX-IX band. The solid lines are fit to the data by Eqs. (2) (left column) and (1) (right column) of the main text. **b** Summary of the estimated rise times $\tau_r$ as a function of $P_{exc}$. Above 1 $\mu$m (as highlighted by the vertical dashed line) the rise time goes below the resolution limit of our setup. **c** Summary of the estimated decay times $\tau_{d,n}$ as a function of $P_{exc}$ and corresponding weights $w_{d,n}$.

**Table 4.1:** Fitting parameter values shown in Fig. 4.2**b**. $\tau_{d,n}$ is the decay time relative to the $n$-th component, whose weight is given by $w_{d,n}$. The last column reports the weighted decay time $\tau$.

| $P_{exc}$ (nW) | $\tau_{d,1}$ (ns) | $w_{d,1}$ | $\tau_{d,2}$ (ns) | $w_{d,2}$ | $\tau_{d,3}$ (ns) | $w_{d,3}$ | $\tau$ (ns) |
|---|---|---|---|---|---|---|---|
| 10 | 9.3 | 0.32 | 60.2 | 0.34 | 254.9 | 0.34 | 110.4 |
| 20 | 10 | 0.36 | 56.2 | 0.34 | 242.0 | 0.31 | 97.1 |
| 44 | 7.2 | 0.46 | 46.3 | 0.36 | 216.4 | 0.19 | 60.0 |
| 100 | 5.3 | 0.50 | 38.4 | 0.32 | 201.2 | 0.17 | 49.9 |
| 200 | 3.7 | 0.64 | 32.7 | 0.26 | 180.9 | 0.10 | 29.8 |
| 440 | 3.0 | 0.68 | 27.5 | 0.23 | 171.4 | 0.08 | 22.9 |
| 1000 | 2.3 | 0.73 | 24.1 | 0.20 | 170.8 | 0.06 | 17.6 |
| 2000 | 2.1 | 0.77 | 22.6 | 0.18 | 159.2 | 0.05 | 13.7 |
| 3000 | 1.5 | 0.81 | 19.1 | 0.15 | 150.7 | 0.04 | 9.9 |

Given the results shown in Figs. 4.1 and 4.3, we can solve Eq. 4.3 –namely $n_{e-h}=G(n_{e-h}) \cdot \tau(n_{e-h})$– numerically as displayed in Fig. 4.4. The solutions are given by the crossing of the first and second member of the above equation plotted on the $y$ and $x$ axis, respectively. That plot finally allows us to give the density of photogenerated electron-hole pairs for a specific excitation power $P_{exc}$.

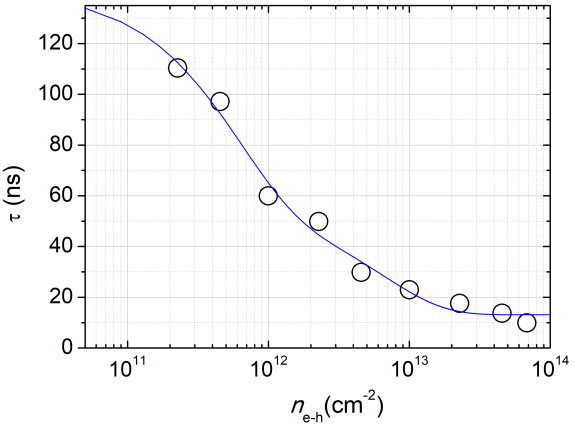


**Figure 4.3:** Dependence of the weighted decay time $\tau$ (symbols; see Table 4.1) on the density of photogenerated carriers $n_{\mathrm{e-h}}$. The solid line is a bi-exponential fit used to interpolate the data.

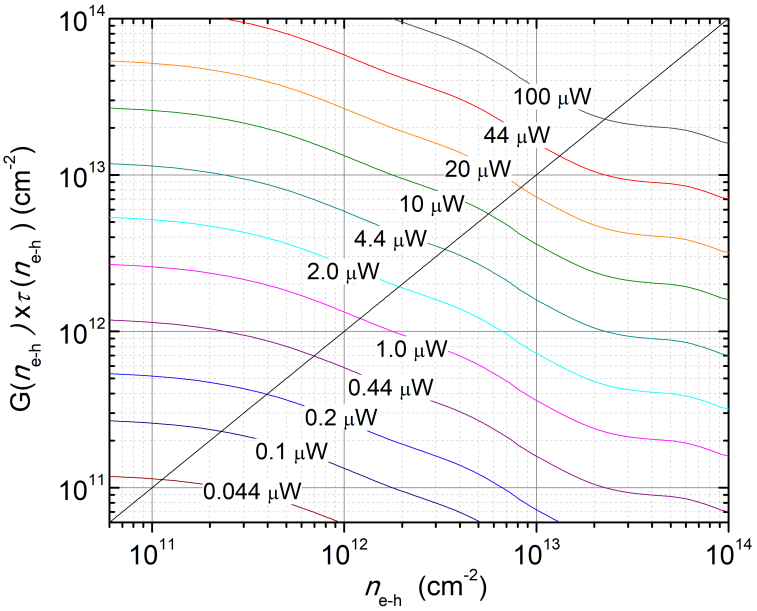


**Figure 4.4:** Plot of $G(n_{\mathrm{e-h}}) \cdot \tau(n_{\mathrm{e-h}})$ *vs* $n_{\mathrm{e-h}}$. The intersections between the bisecting black line and the other curves gives the solutions of Eq. 4.2 for each of the cw $P_{\mathrm{exc}}$ values considered in Fig. 3**a** of the main text.

## Supplementary Note 5. Time-resolved micro-photoluminescence *vs* power at low temperature

Analogous measurements to those discussed in Supplementary Note 4 for HS1 were performed also for HS2. In particular, we performed time-resolved $\mu$-PL measurements at 6 K by varying the excitation power over more than two orders of magnitude. The decay times and corresponding weights estimated for HS1 and HS2 and displayed and compared in Fig. 5.1. Indeed, very similar

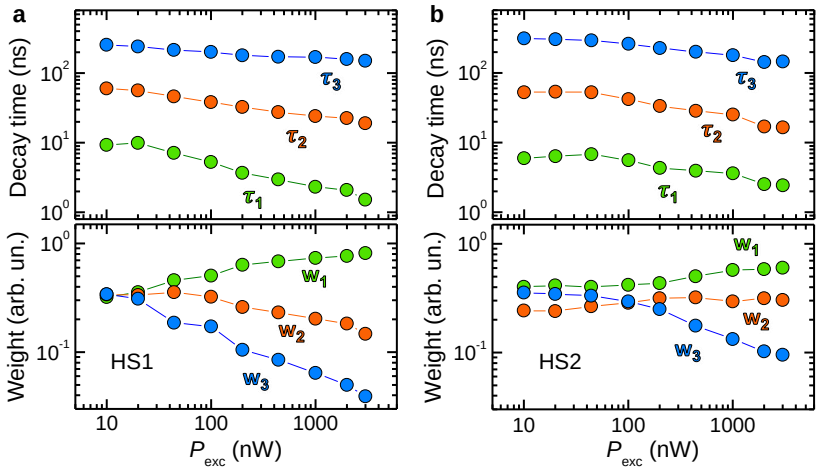


**Figure 5.1:** Decay times and weights derived from time-resolved $\mu$-PL measurements performed at 6 K for different excitation powers $P_{\mathrm{exc}}$. The data were acquired in the $\Delta t$=0-800 ns interval from the laser pulse. The detection energy was set at the MX-IX band. **a** Summary of the estimated decay times $\tau_{\mathrm{d,n}}$ as a function of $P_{\mathrm{exc}}$ (top) and corresponding weights $w_{\mathrm{d,n}}$ (bottom), for HS1. **b** Same for HS2.

trends are observed for both HS1 and HS2, with HS2 generally showing slightly slower decay times due to the slightly larger twist angle (see Supplementary Note 2).

## Supplementary Note 6. Integrated photoluminescence intensity of HS1 *vs* power density for different temperatures

The data shown in Fig. 3**c** of the main text were derived by fitting the PL integrated intensity $I$ of HS1 at different temperatures using the following equation

$$I = A \cdot P_{\text{exc}}^{\alpha}, \tag{6.1}$$

where $P_{\text{exc}}$ is the laser excitation power, $A$ is a scaling constant and $\alpha$ a coefficient, whose value suggests the type of transition involved (*e.g* $\alpha$=1 exciton transition, $\alpha$=2 uncorrelated electron-hole pairs, $\alpha$<1 finite density two-level system). Figure 6.1 shows the dependence of $I$ on $P_{\text{exc}}$ for the two main bands observed MX-IX (interlayer exciton, either moiré, MX, or free, IX) and X (free exciton of the heterostructure constituents); see, *e.g.* Figs 2 (a) and 3 (a) in the main text. The measurements were performed at different temperatures between 6 K and 296 K. The results of the fits are displayed in the different panels of Figure 6.1.

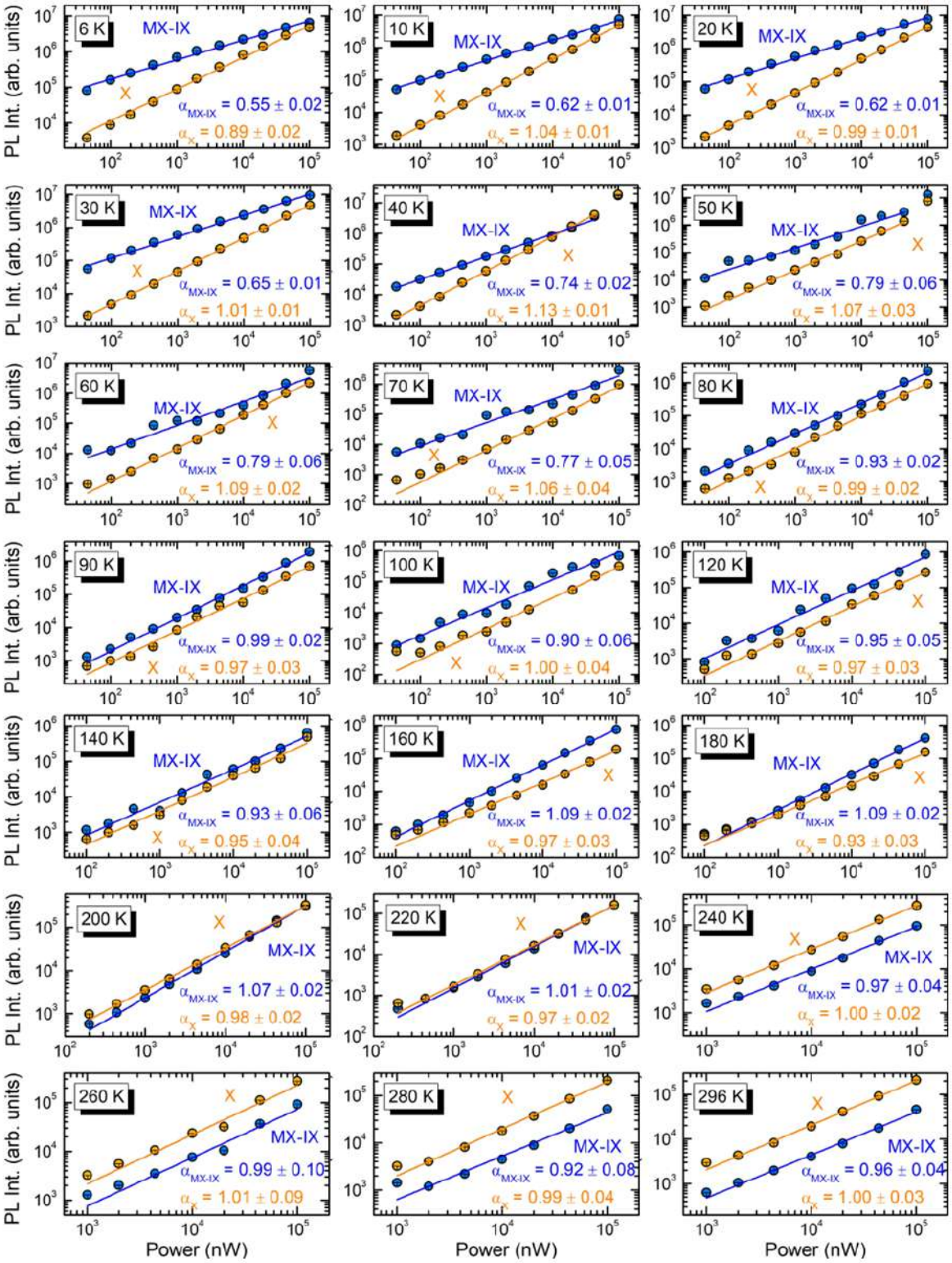


**Figure 6.1:** PL integrated intensity dependence on the laser power for MX-IX (azure symbols) and X (dark yellow symbols) bands at different temperatures for HS1. Solid lines are fits to the data via Eq. 6.1. The $\alpha$ coefficient values obtained from the fits are displayed within each plot.

## Supplementary Note 7. Integrated photoluminescence intensity of HS2 *vs* power density for different temperatures

Fig. 3 of the main text and Supplementary Note 6 clearly show the transition from a localised to a delocalised regime for the interlayer exciton when increasing temperature, which is evidenced by power-dependent $\mu$-PL studies on HS1. To ensure the general validity of our statements, we repeated analogous measurements on HS2. As noted in Fig. 3**d** of the main text, at intermediate temperatures of about 90 K a dramatic lineshape change can be observed when increasing power, showing a clear transition from the MX prevailing at low $P_{\text{exc}}$ to the IX prevailing at high $P_{\text{exc}}$. The same trend was indeed observed also for HS2, as demonstrated by the power-dependent spectra acquired at 80 K and shown in Fig. 7.1.

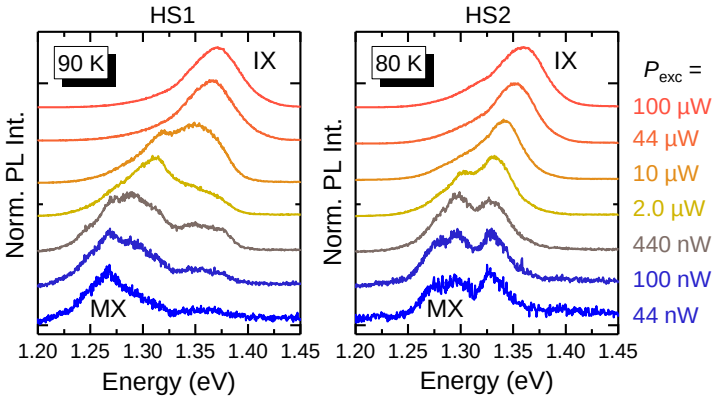


**Figure 7.1:** Left: $T$=90 K $\mu$-PL spectra of HS1 for different laser excitation powers in the energy region where the MX and IX recombinations can be simultaneously observed. IX takes over MX upon increase of the photo-generated carrier density. Right: Same at $T$=80 K for HS2.

Power-dependent measurements were performed at different temperatures between 6 K and 296 K, analogously to HS1. The integrated PL intensity of the MX/IX and of the X band were then analysed and fitted by Eq. 3 of the main text, leading to the $\alpha$ coefficients shown in Fig. 7.2.

Similarly to HS1, also for HS2 one can notice a saturation behaviour (evidenced by the sublinear power trend, *i.e.*, $\alpha < 1$) of the MX/IX band at low temperatures, with the $\alpha$ coefficient that increases with temperature. From about 100 K, the power trend becomes linear ($\alpha = 1$). Interestingly, for HS2 the linear trend is reached at a $T$ value about 20 K lower than for HS1 (as highlighted by the black dashed lines is Fig. 7.2), consistently with the shallower moiré potential expected for larger twist angles.

The whole set of data concerning the dependence of the PL integrated intensity $I$ of HS2 on $P_{\text{exc}}$ for the MX-IX and X bands and the corresponding fits, from which the $\alpha$ coefficients were derived, is shown in Fig. 7.3.

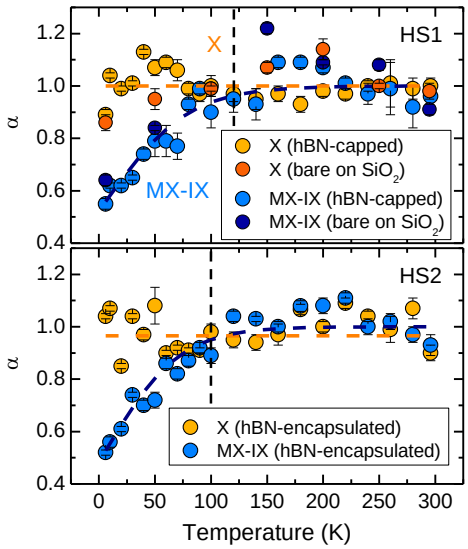


**Figure 7.2:** Temperature variation of the $\alpha$ coefficient for the MX-IX and X bands, comparison between HS1 and HS2. For HS1, some points measured before hBN-capping were also included in the plot, showing that the data agree well with those acquired after hBN-capping. Both for HS1 and HS2, a clear transition from a sublinear to a linear behaviour is found for the MX-IX band, which is ascribed to the transition from a moiré localisation regime to a free interlayer exciton one. Such a transition occurs at $\approx 120$ K for HS1, and for $\approx 100$ K for HS2, as highlighted by the black dashed lines.

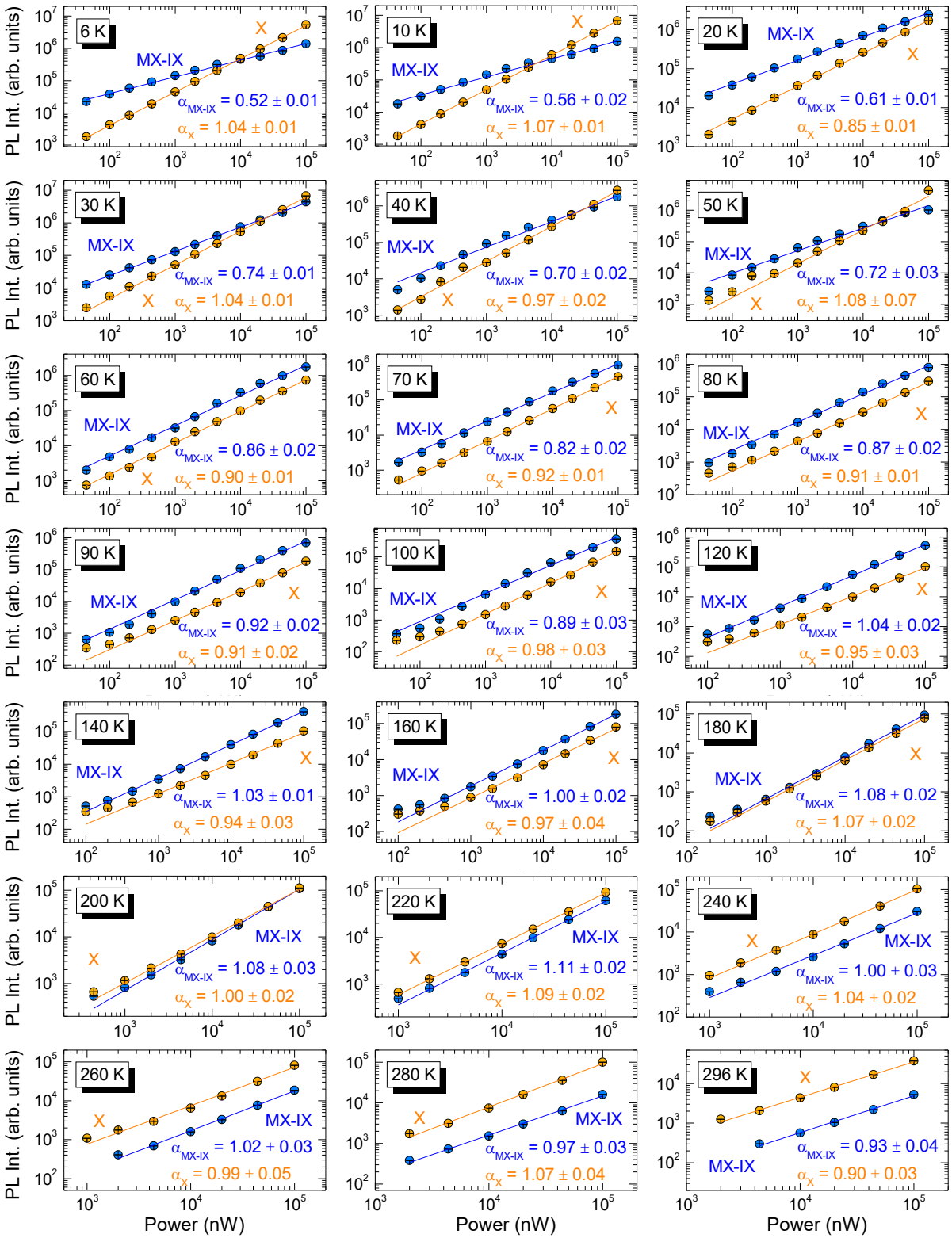


**Figure 7.3:** PL integrated intensity dependence on the laser power for MX-IX (azure symbols) and X (dark yellow symbols) bands at different temperatures for HS2. Solid lines are fits to the data via Eq. 6.1. The $\alpha$ coefficient values obtained from the fits are displayed within each plot.

## Supplementary Note 8. Temperature-dependent micro-photoluminescence

Figure 4**a** in the main text shows the temperature dependence of the $\mu$-photoluminescence (PL) spectra recorded on the investigated $WSe_2/MoSe_2$ heterostructure for a given laser excitation power $P_{exc}$ (=10 $\mu$W). The set of data shows a clear $T$-induced variation in the emission lineshape caused by the de-trapping of moiré-localised excitons (MXs) in favour of free interlayer excitons (IXs). Figure 8.1 shows a similar study performed at a higher (=100 $\mu$W) and lower (=1 $\mu$W) $P_{exc}$. Figure 8.1 indicates that, for a given $T$, the de-trapping process becomes more apparent for a larger density of photogenerated carriers (*i.e.* larger $P_{exc}$).

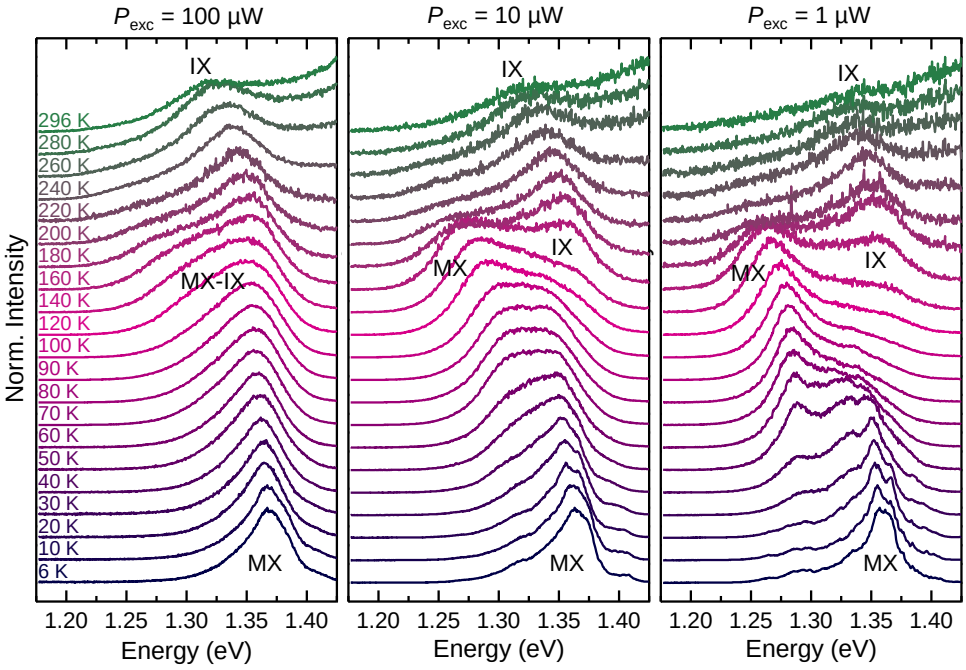


**Figure 8.1:** $\mu$-PL spectra *vs* $T$ at three different laser excitation powers $P_{exc}$ (focused via a 20× objective with NA = 0.4). MX and IX indicate the recombination band due to moiré-localised excitons (MXs) and free interlayer excitons (IXs), respectively.

This can be better appreciated in Figure 8.2. Indeed, for fixed $T$=160 K, the relative weight of the IX component increases for increasing number of photogenerated carriers and for the ensuing saturation of the finite moiré potential sites. This saturation takes place more evidently as $T$ increases, which favours moiré de-trapping as shown in the previous figure.

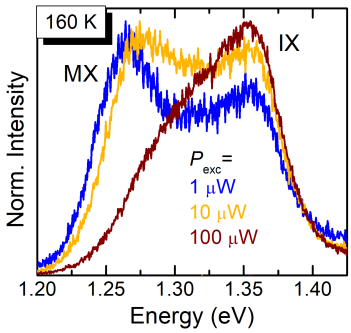


**Figure 8.2:** $\mu$-PL spectra at 160 K for different laser excitation powers $P_{exc}$ (focused via a 20× objective with NA = 0.4). MX and IX indicate the recombination band due to moiré-localised excitons (MXs) and free interlayer excitons (IXs), respectively.

## Supplementary Note 9. $g$-factor of moiré and free interlayer excitons in HS2

Fig. 4 of the main text shows the result of magneto-$\mu$-PL measurements performed on HS1 at low power and low $T$ —to measure the $g$-factor of MX lines— and at high power and high $T$ —to measure the $g$-factor of free interlayer excitons. To ensure the general validity of our results, we performed similar measurements on HS2. Fig. 9.1**a** shows the polarisation-resolved magneto-$\mu$-PL spectra acquired on HS2 at 10 K with $P_{\text{exc}} = 50$ nW, while varying the magnetic field from 0 to 16 T in steps of 0.5 T. While the field increases, the energy of the narrow lines (see, *e.g.*, lines denoted as M1 and M2) is higher for the $\sigma^+$ polarisation with respect to the $\sigma^-$ one, and the $g$-factor is thus positive. Fig. 9.1**b** shows instead the spectra acquired at 160 K with $P_{\text{exc}} = 100$ $\mu$W. The spectra were acquired while increasing the field from 0 to 12 T in steps of 0.5 T (only some spectra are shown in the figure for ease of visualisation). In this case, the IX can be observed, and the $\sigma^-$ component lies at higher energy than the $\sigma^+$ component, indicating a negative $g$-factor.

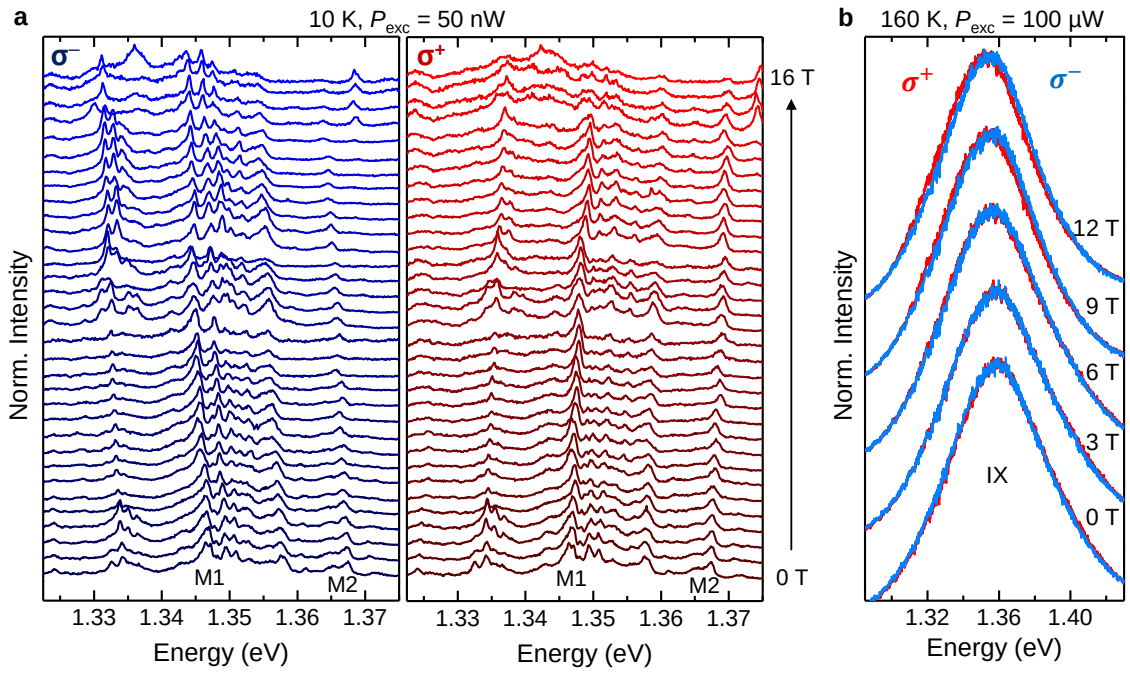


**Figure 9.1:** Magneto-$\mu$-PL measurements on HS2 at low and high $T$s. **a** Polarisation-resolved magneto-$\mu$-PL spectra acquired on HS2 with $P_{\text{exc}} = 50$ nW from 0 to 16 T in steps of 0.5 T. Two moiré narrow lines (Ms) are indicated. **b** Polarisation-resolved magneto-$\mu$-PL spectra at $T = 160$ K and $P_{\text{exc}}$=100 $\mu$W of the free IX band for $\sigma^+$ and $\sigma^-$ polarisations. A negative ZS can be observed, with the $\sigma^+$ and $\sigma^-$ spectra being at lower and higher energy, respectively.

A quantitative analysis of the $g$-factor of the moiré narrow lines M1 and M2 at 10 K and of the IX band at 160 K is shown in Fig. 9.2. The $g$-factor values estimated for HS2 are indeed very close to those found for HS1 and displayed in Fig. 4**d** of the main text.

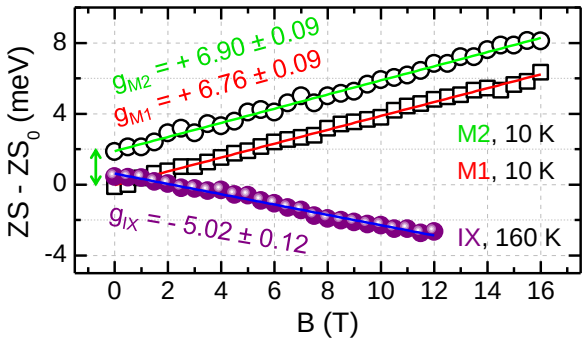


**Figure 9.2:** $g$-factor of the MXs and IX of HS2. **d** ZS of the two moiré-localised excitons M1 and M2 highlighted in Fig. 9.1**a** and of the free IX exciton shown in Fig. 9.1**b** *vs* magnetic field, resulting in the $g$-factors displayed in the figure. The ZS data of the M2 line was shifted by y-offset (by 2 meV) for ease of visualisation.

## Supplementary Note 10. $g$-factor of the moiré energy levels

Fig. 10.1 shows the polarisation-resolved magneto-$\mu$-PL spectra acquired on HS1 as a function of the magnetic field, with excitation powers as low as 10 nW. The data shown here are the complete set of data from which the plots in Fig. 4**b** of the main text were derived.

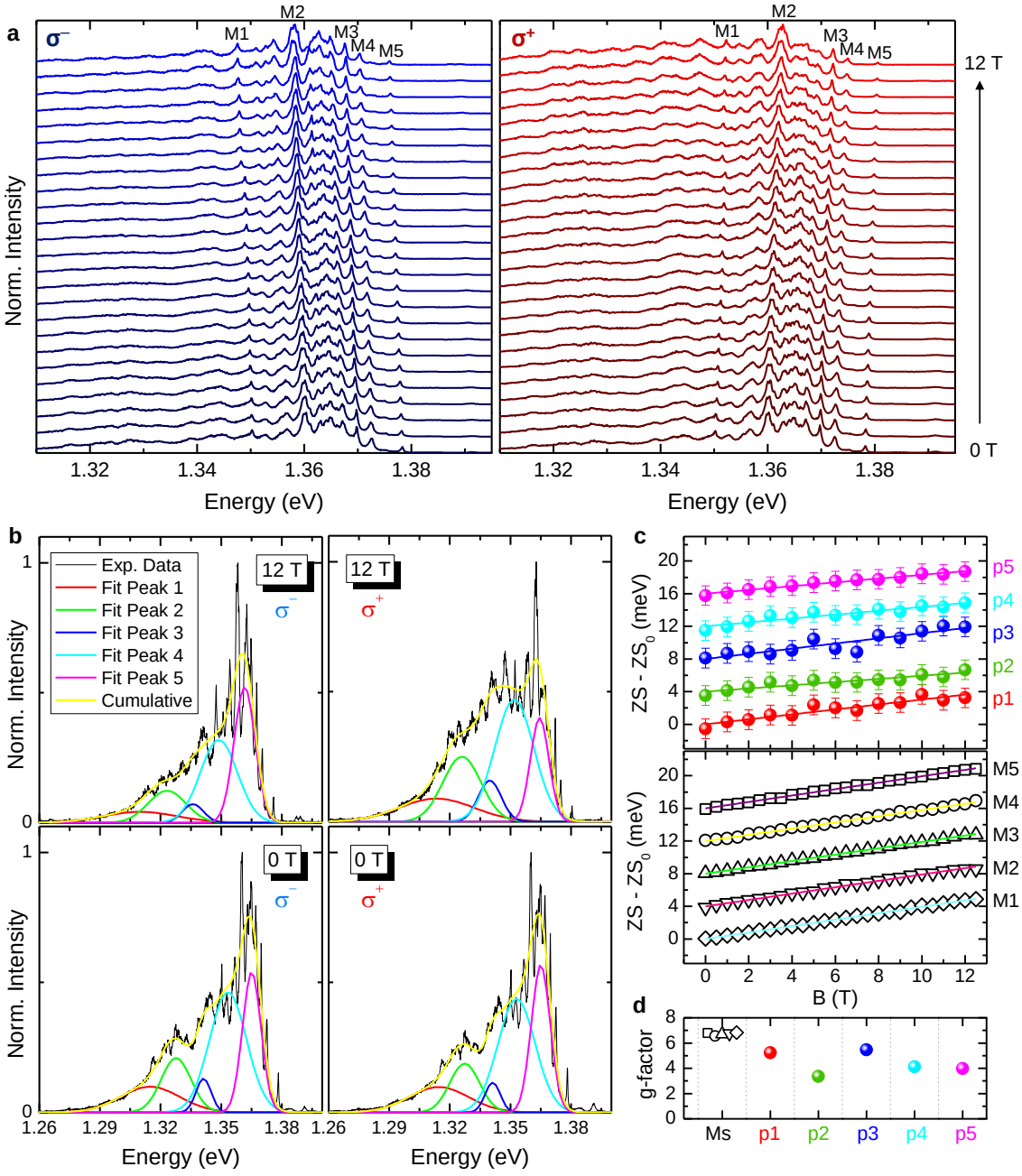


**Figure 10.1:** $g$-factor analysis of the moiré energy levels. **a** Polarisation-resolved magneto-$\mu$-PL spectra acquired on HS1 with $P_{\text{exc}} = 10$ nW from 0 to 12 T in steps of 0.5 T. Five moiré narrow lines (Ms) are indicated. **b** Exemplifying spectra at 12 T and 0 T fitted by 5 gaussian peaks, for both the $\sigma^-$ and $\sigma^+$ polarisations. **c** Top: ZS of the five gaussian peaks (ps) as a function of the magnetic field. The solid lines are linear fits to the data that provide the $g$-factors displayed in panel **d**. The intercept was subtracted from the data and they were stacked by 4 meV for ease of comparison. Bottom: Same for the 5 different moiré narrow lines. **d** Summary of the $g$-factors of both the narrow lines and the gaussian components. The error bars are smaller than (comparable to) the point size for the Ms (ps).

From this set of data, we first measured the $g$-factor of 5 different individual narrow lines (indicated as Ms), finding values between +6.57 and +6.82, see Fig. 10.1. We then fitted the whole set of data with multiple gaussians, as exemplified in panel **b** at 0 and 12 T.

Indeed, the 5 peaks feature a positive $g$-factor, similarly to the moiré single lines, but with smaller absolute value. This might possibly be attributed to the role played by exciton-exciton interactions.

These results are particularly significant since the similar values (sign and modulus) of the $g$-factor of the exciton manifold and of the single lines indicate a common electronic structure/origin of those recombination lines. In particular, it indicates that the narrow lines are indeed single moiré excitons giving rise to a gaussian distribution when a sufficiently high number of them is photogenerated. As a matter of fact, the exact nature of those narrow lines is a topic recently debated in the literature [1, 5].

## Supplementary Note 11. Temperature-dependent $g$-factor of the MX/IX band

Figure 11.1 shows a series of magneto-$\mu$-PL spectra recorded with an excitation power of 75 $\mu$W at different magnetic fields for $T$=210, 160 and 100 K, panels (a), (c) and (e), respectively. The spectra were recorded with opposite circular polarisation filtering ($\sigma^+$ and $\sigma^-$) and the ZS was then derived. The ZS dependence on $B$ is shown in panels (b), (d) and (f) for $T$=210, 160 and 100 K, respectively. At the considered temperatures, $g$ is negative and corresponds to the gyromagnetic factor of the free interlayer exciton $g_{\mathrm{exc,IX}}$. The values found for different $T$s are shown in the corresponding panels and do not change appreciably with temperature. As discussed in the main text, the $g_{\mathrm{exc,IX}}$ sign and absolute value can be ascribed to the avoided action of the moiré potential determined by the $T$-induced MX de-trapping. Indeed, $g_{\mathrm{exc,IX}}$ can be estimated by considering the separate contribution of electrons and holes to the IX gyromagnetic factor (see Eq. (5) in the main text).

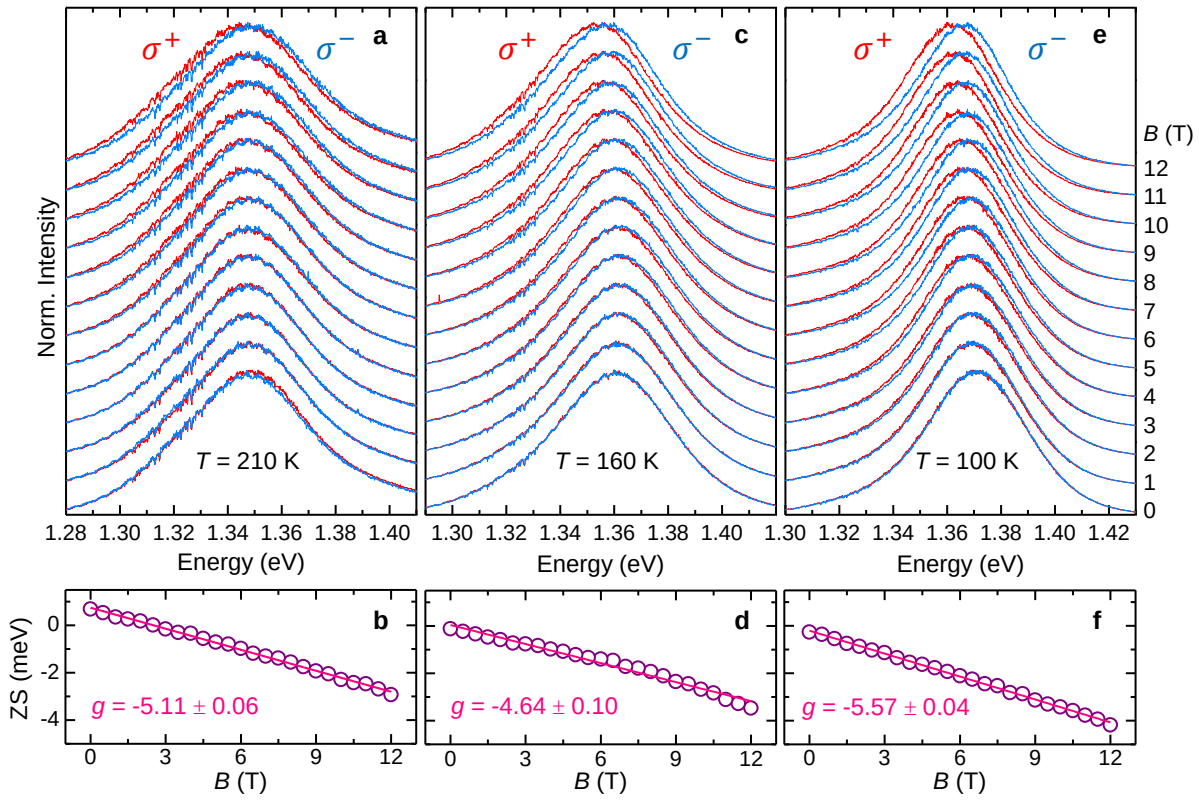


**Figure 11.1:** **a** Helicity-resolved normalised $\mu$-PL spectra *vs* magnetic field at $T = 210$ K. **b** ZS of the band, from which the displayed $g$-factor was obtained through a linear fit. **c-d** Same as panels **a-b** for $T = 160$ K. **e-f** Same as panels **a-b** for $T = 100$ K. It should be noticed that the standard deviation associated to each fit clearly underestimates the real error on the $g$-factor. The latter is in fact a bit dependent on the exact sample position where the measurements are taken. By staying at the maximum field (12 T) and changing position, we observed ZS variations within 20-25 %. The results of panels **b**, **d** and **f** thus show that within the position-related uncertainty, a similar $g$-factor of $\approx +5$ is found at elevated temperatures. The same excitation power $P_{\mathrm{exc}} = 75$ $\mu$W (focused via a 100× objective with NA = 0.8) was used for all the sets of data.

To further prove the localised-to-delocalised transition of interlayer excitons with temperature, we recorded magneto-$\mu$-PL spectra at various intermediate temperatures, where the MX and IX coexist. However, disentangling the contribution of the overlapping MX and IX bands in the spectrum is not feasible, especially considering the necessity of using high laser powers to attain a sizable PL signal. This inevitably leads to a prevailing signal form the free IX band. We thus performed high-field (16 T) magneto-$\mu$-PL measurements at a relatively high $T$ of 80

K aimed at highlighting the MX component with respect to the free IX band. To do so, we employed very low laser powers of 10 nW. The results are shown in Fig. 11.2. We acquired the

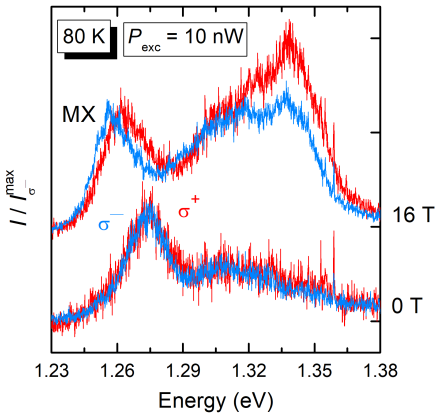


**Figure 11.2:** Polarisation-resolved magneto-$\mu$-PL spectra acquired at 0 and 16 T on HS1 with a power as low as 10 nW, in order to highlight the MX contribution. The low energy peak, attributed to the MX, shows a clear positive Zeeman splitting. At each field, the MX peak of the $\sigma^-$ component is normalised to 1.

spectra at 0 T and 16 T (a whole sweep was not feasible because of the very low PL signal due to the low power and high $T$ employed) and observed a clear splitting of the MX band at 16 T, from which we derive an estimate of the $g$-factor of about +6. The data agree with previous assignments demonstrating that the positive gyromagnetic factor for MX is indeed found also at 80 K.

## Supplementary Note 12. Power studies of the MX/IX band at 16 T and low $T$

Here we discuss additional magneto-$\mu$-PL measurements on HS1 and HS2 employing a fixed magnetic field $B$ of 16 T, with $P_{\mathrm{exc}}$ values ranging over five orders of magnitude. The results are shown in Fig. 12.1. With increasing $P_{\mathrm{exc}}$ (or equivalently $n_{\mathrm{e-h}}$), the positive Zeeman splitting (*i.e.*, $E^{\sigma^+}>E^{\sigma^-}$) of the narrow emission lines related to various moiré-confined excitons (see, *e.g.*, the narrow lines highlighted by the black circles at the lowest $P_{\mathrm{exc}}$) becomes nearly zero as the PL band broadens and eventually turns negative on the high energy side of the $\mu$-PL spectrum at the highest $P_{\mathrm{exc}}$ used. Thus, the high density of excitons achieved for large $P_{\mathrm{exc}}$ leads to an increased intercell exciton hopping [21], and to an ensuing sizable contribution from de-trapped moiré excitons to the emission spectrum that reflects in the change of lineshape (the appearance of a high energy contribution can be noticed) and especially in the change of sign of $g_{\mathrm{exc}}$. This can be noticed especially for HS1. For HS2, the $g$-factor at high power is negative but small, presumably due to a coexistence of localised states and free excitons at the largest power we used.

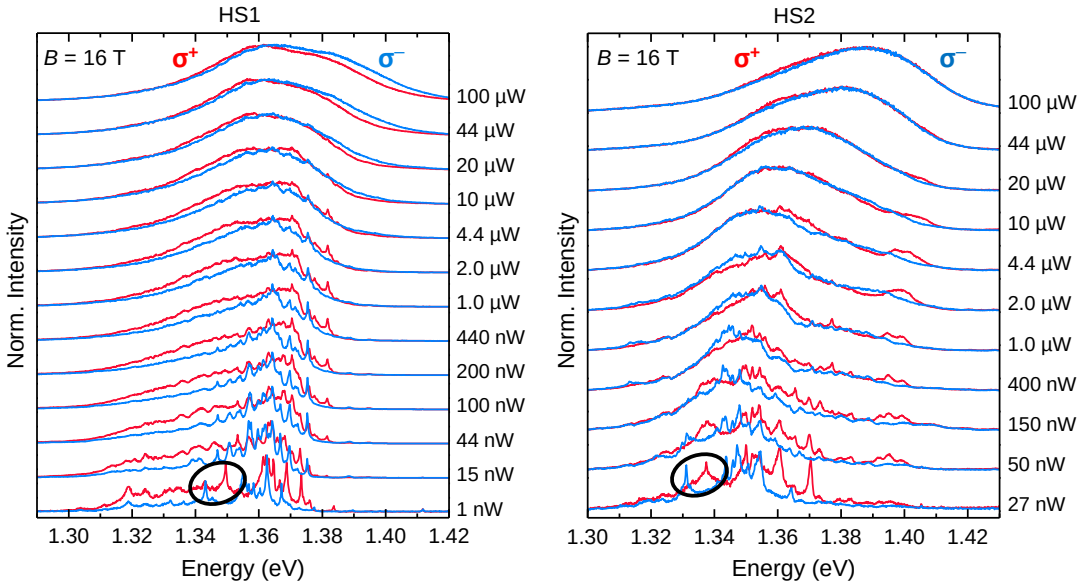


**Figure 12.1:** Polarisation-resolved $\mu$-PL power studies performed at 10 K under a 16 T magnetic field for both HS1 and HS2. At low powers, several Zeeman-split narrow lines can be observed, such as those highlighted by the black circle. At high powers, a change in the sign of the Zeeman splitting can clearly be noticed.

## References


[1] F. Mahdikhanysarvejahany, D. N. Shanks, M. Klein, Q. Wang, M. R. Koehler, D. G. Mandrus, T. Taniguchi, K. Watanabe, O. L. Monti, B. J. LeRoy, and J. R. Schaibley, *Localized Interlayer Excitons in $MoSe_2/WSe_2$ Heterostructures without a Moiré Potential*, ArXiv e-prints p. arXiv:2203.08052 (2022).

[2] E. Liu, E. Barré, J. van Baren, M. Wilson, T. Taniguchi, K. Watanabe, Y.-T. Cui, N. M. Gabor, T. F. Heinz, Y.-C. Chang, and C. H. Lui, *Signatures of moiré trions in $MoSe_2/WSe_2$ heterobilayers*, Nature **594**, 46 (2021).

[3] T. Wang, S. Miao, Z. Li, Y. Meng, Z. Lu, Z. Lian, M. Blei, T. Taniguchi, K. Watanabe, S. Tongay, D. Smirnov, and S.-F. Shi, *Giant Valley-Zeeman Splitting from Spin-Singlet and Spin-Triplet Interlayer Excitons in $WoSe_2/MoSe_2$ Heterostructure*, Nano Lett. **20**, 694 (2020).

[4] F. Mahdikhanysarvejahany, D. N. Shanks, C. Muccianti, B. H. Badada, I. Idi, A. Alfrey, S. Raglow, M. R. Koehler, D. G. Mandrus, T. Taniguchi, K. Watanabe, O. L. A. Monti, H. Yu, B. J. LeRoy, and J. R. Schaibley, *Temperature dependent moiré trapping of interlayer excitons in $MoSe_2$-$WSe_2$ heterostructures*, npj 2D Mater. Appl. **5**, 67 (2021).

[5] Z. Li, X. Lu, D. F. C. Leon, Z. Lyu, H. Xie, J. Hou, Y. Lu, X. Guo, A. Kaczmarek, T. Taniguchi, K. Watanabe, L. Zhao, L. Yang, and P. B. Deotare, *Interlayer Exciton Transport in $MoSe_2/WSe_2$ Heterostructures*, ACS Nano **15**, 1539 (2021).

[6] H. Kim, D. Dong, Y. Okamura, K. Shinokita, K. Watanabe, T. Taniguchi, and K. Matsuda, *Dynamics of Moiré Trion and Its Valley Polarization in a Microfabricated $WSe_2/MoSe_2$ Heterobilayer*, ACS Nano **17**, 13715 (2023).

[7] B. Miller, A. Steinhoff, B. Pano, J. Klein, F. Jahnke, A. Holleitner, and U. Wurstbauer, *Long-Lived Direct and Indirect Interlayer Excitons in van der Waals Heterostructures*, Nano Lett. **17**, 5229 (2017).

[8] M. Brotons-Gisbert, H. Baek, A. Campbell, K. Watanabe, T. Taniguchi, and B. D. Gerardot, *Moiré-Trapped Interlayer Trions in a Charge-Tunable $WSe_2/MoSe_2$ Heterobilayer*, Phys. Rev. X **11**, 031033 (2021).

[9] J. Wang, J. Ardelean, Y. Bai, A. Steinhoff, M. Florian, F. Jahnke, X. Xu, M. Kira, J. Hone, and X.-Y. Zhu, *Optical generation of high carrier densities in 2D semiconductor heterobilayers*, Sci. Adv. **5**, eaax0145 (2019).

[10] K. Tran, G. Moody, F. Wu, X. Lu, J. Choi, K. Kim, A. Rai, D. A. Sanchez, J. Quan, A. Singh, J. Embley, A. Zepeda, M. Campbell, T. Autry, T. Taniguchi, K. Watanabe, N. Lu, S. K. Banerjee, K. L. Silverman, S. Kim, E. Tutuc, L. Yang, A. H. MacDonald, and X. Li, *Evidence for moiré excitons in van der Waals heterostructures*, Nature **567**, 7746, 71–75 (2019).

[11] W. Li, X. Lu, J. Wu, and A. Srivastava, *Optical control of the valley Zeeman effect through many-exciton interactions*, Nat. Nanotechnol. **16**, 148 (2021).

[12] K. L. Seyler, P. Rivera, H. Yu, N. P. Wilson, E. L. Ray, D. G. Mandrus, J. Yan, W. Yao, and X. Xu, *Signatures of moiré-trapped valley excitons in $MoSe_2/WSe_2$ heterobilayers*, Nature **567**, 66 (2019).

[13] W. Li, X. Lu, S. Dubey, L. Devenica, and A. Srivastava, *Dipolar interactions between localized interlayer excitons in van der Waals heterostructures*, Nat. Mater. **19**, 624 (2020).

[14] J. Choi, M. Florian, A. Steinhoff, D. Erben, K. Tran, D. S. Kim, L. Sun, J. Quan, R. Claassen, S. Majumder, J. A. Hollingsworth, T. Taniguchi, K. Watanabe, K. Ueno, A. Singh, G. Moody, F. Jahnke, and X. Li, *Twist Angle-Dependent Interlayer Exciton Lifetimes in van der Waals Heterostructures*, Phys. Rev. Lett. **126**, 047401 (2021).

[15] H. Baek, M. Brotons-Gisbert, Z. X. Koong, A. Campbell, M. Rambach, K. Watanabe, T. Taniguchi, and B. D. Gerardot, *Highly energy-tunable quantum light from moiré-trapped excitons*, Sci. Adv. **6**, 37, eaba8526 (2020).

[16] M. Troue, J. Figueiredo, L. Sigl, C. Paspalides, M. Katzer, T. Taniguchi, K. Watanabe, M. Selig, A. Knorr, U. Wurstbauer, and A. W. Holleitner, *Extended Spatial Coherence of Interlayer Excitons in $MoSe_2/WSe_2$ Heterobilayers*, Phys. Rev. Lett. **131**, 036902 (2023).

[17] P. Parzefall, J. Holler, M. Scheuck, A. Beer, K.-Q. Lin, B. Peng, B. Monserrat, P. Nagler, M. Kempf, and T. Korn, *Moiré phonons in twisted $MoSe_2$-$WSe_2$ heterobilayers and their correlation with interlayer excitons*, 2D Materials **8**, 035030 (2021).

[18] H. Kim, K. Aino, K. Shinokita, W. Zhang, K. Watanabe, T. Taniguchi, and K. Matsuda, *Dynamics of Moiré Exciton in a Twisted $MoSe_2/WSe_2$ Heterobilayer*, Adv. Optical Mater. **11**, 2300146 (2023).

[19] M. R. Rosenberger, H.-J. Chuang, M. Phillips, V. P. Oleshko, K. M. McCreary, S. V. Sivaram, C. S. Hellberg, and B. T. Jonker, *Twist Angle-Dependent Atomic Reconstruction and Moiré' Patterns in Transition Metal Dichalcogenide Heterostructures*, ACS Nano **14**, 4550 (2020).

[20] F. Wu, T. Lovorn, and A. H. MacDonald, *Theory of optical absorption by interlayer excitons in transition metal dichalcogenide heterobilayers*, Phys. Rev. B **97**, 035306 (2018).

[21] S. Brem and E. Malic, *Bosonic Delocalization of Dipolar Moiré Excitons*, Nano Lett. **23**, 4627 (2023).